

MeDUET: Disentangled Unified Pretraining for 3D Medical Image Synthesis and Analysis

Junkai Liu¹, Ling Shao², Le Zhang¹

¹School of Engineering, University of Birmingham, UK

²UCAS-Terminus AI Lab, University of Chinese Academy of Sciences, Beijing, China

jx11920@student.bham.ac.uk; l.zhang.16@bham.ac.uk

Abstract

Self-supervised learning (SSL) and diffusion models have advanced representation learning and image synthesis. However, in 3D medical imaging, they remain separate: diffusion for synthesis, SSL for analysis. Unifying 3D medical image synthesis and analysis is intuitive yet challenging, as multi-center datasets exhibit dominant style shifts, while downstream tasks rely on anatomy, and site-specific style co-varies with anatomy across slices, making factors unreliable without explicit constraints. In this paper, we propose MeDUET, a 3D Medical image Disentangled Unified PreTraining framework that performs SSL in the Variational Autoencoder (VAE) latent space which explicitly disentangles domain-invariant content from domain-specific style. The token demixing mechanism serves to turn disentanglement from a modeling assumption into an empirically identifiable property. Two novel proxy tasks, Mixed-Factor Token Distillation (MFTD) and Swap-invariance Quadruplet Contrast (SiQC), are devised to synergistically enhance disentanglement. Once pretrained, MeDUET is capable of (i) delivering higher fidelity, faster convergence, and improved controllability for synthesis, and (ii) demonstrating strong domain generalization and notable label efficiency for analysis across diverse medical benchmarks. In summary, MeDUET converts multi-source heterogeneity from an obstacle into a learning signal, enabling unified pretraining for 3D medical image synthesis and analysis. The code is available at <https://github.com/JK-Liu7/MeDUET>.

1. Introduction

Recently, self-supervised learning (SSL) following the pretraining-finetuning paradigm has emerged as a powerful approach, significantly improving performance across diverse downstream applications [7, 28, 29, 53]. Meanwhile, image generation has seen remarkable progress with

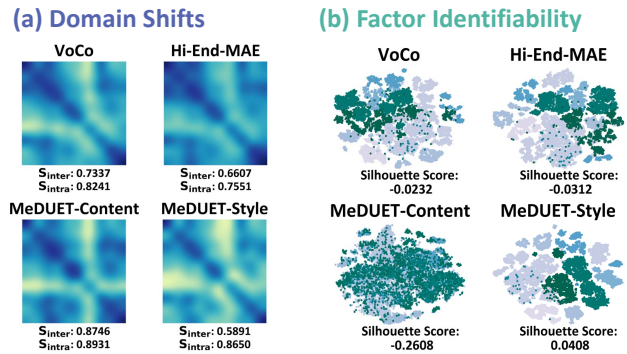


Figure 1. The **motivation** of our proposed MeDUET. (a) Latent similarity heatmap across domains (S_{inter} / S_{intra} : inter-/intra-domain similarity). Compared with baseline medical SSL, which exhibits site-driven feature blocks, MeDUET isolates *domain shifts* within the style map while maintaining a uniformly consistent content map across domains. (b) Latent t-SNE colored by domain. The baseline SSL clusters embeddings primarily by domain rather than anatomy, indicating style-dominated representations, whereas MeDUET disentangles content and style in separate embedding spaces, enhancing *factor identifiability*.

diffusion models [17, 34, 60]. Motivated by the intuition that generative modeling can foster a deeper understanding of visual data, pioneering studies [78, 82] have shown that diffusion models possess outstanding representational capability for perception tasks. In medical AI, both SSL and generative models have attracted considerable attention for 3D medical image synthesis [25, 69] and analysis [4, 79], respectively. Nonetheless, the potential of diffusion models in medical perception tasks, i.e., unified pretraining for both generation and understanding, remains largely unexplored. Inspired by prior work [14], we ask the following research question: *How can we establish a unified pretraining framework that benefits both 3D medical image synthesis and analysis tasks?*

Real-world 3D medical datasets aggregate heterogeneous sites, scanners, field strengths, sequences, and co-

horts [4, 79, 80], amplifying **domain shifts** mainly at the *style* level. For example, a liver CT model trained on Hospital A (Siemens, 120 kVp, venous, 2.5 mm, soft kernel) degrades on Hospital B (GE, 100 kVp, arterial, 1.0 mm, sharp) because HU histograms, noise, and edge profiles change while anatomy does not. In contrast, downstream tasks rely on *content* such as organ topology, lesion morphology, and anatomical continuity [44, 54]. A naïve unification of synthesis and analysis entangles style and anatomy, reducing generator controllability and causing perception models to overfit to style cues, which weakens generalization and label efficiency [52, 67]. Thus, domain generalization is vital for unified pretraining but remains underexplored in current SSL frameworks (Fig. 1(a)) [65, 68, 70, 90].

In light of this challenge and opportunity, we formalize each volume as composed of two factors, a domain-invariant *content* factor that encodes intrinsic anatomy and captures stable semantics across domains, and a domain-specific *style* that reflects acquisition conditions and visual appearance, accounts for peripheral, domain-varying changes [5, 23, 52, 90]. However, clinical style differences are often subtle or even imperceptible, where the same structure can look different across centers while its geometry is unchanged, making **factor identifiability** non-trivial for reliable encoding (Fig. 1(b)) [44, 85]. For instance, in contrast-enhanced CT, hyperattenuation may stem from true lesion enhancement (content) or from contrast timing, kVp, or reconstruction kernel (style). Without explicit disentanglement, multiple content and style explanations can account for the same image, rendering the factors unidentifiable.

Motivated by the above analysis, we present MeDUET, a 3D Medical image **Disentangled UniFiEd PreTraining** model performed in the VAE latent space, facilitating both synthesis and analysis (Fig. 2(a)). This latent space enables compact spatial tokenization of 3D volumes while naturally interfacing with latent diffusion. Our key insight is to reconcile the distinct goals of generation and perception by explicitly disentangling latent tokens into a domain-invariant content pathway and a domain-specific style pathway. Opposing task objectives encourage content tokens to be domain-invariant while style tokens capture acquisition-related variations. To ensure practical identifiability, a demixing module simulates “shared anatomy, different styles,” yielding more robust features than masked reconstruction. Two complementary pretext tasks reinforce the learning signals on the factorized tokens: Mixed Factor Token Distillation (MFTD) guides inference at mixed positions via teacher signals, and Swap-invariance Quadruplet Contrast (SiQC) enforces within-factor consistency under content-style swaps while preserving inter-factor discriminability. The pretrained MeDUET can be seamlessly adapted to both synthesis and analysis tasks, providing a

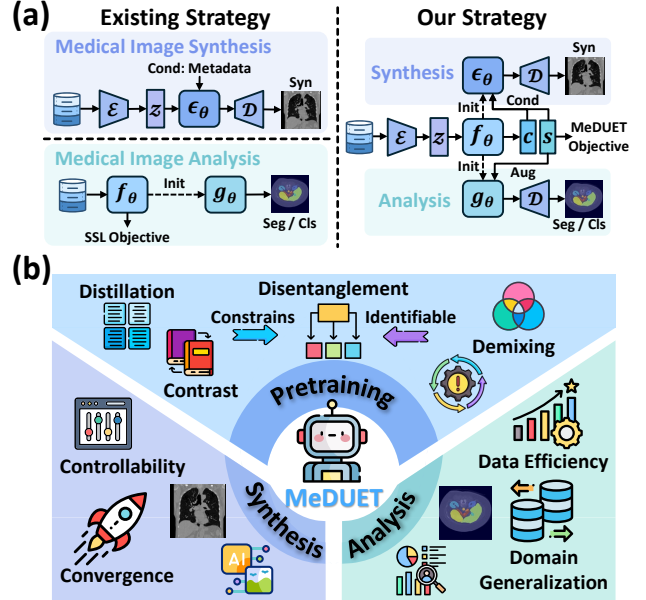


Figure 2. (a) **Comparison** between existing medical image synthesis/analysis paradigms and our unified strategy. (b) **Overview** of our proposed MeDUET.

strong weight initialization for both applications (Fig. 2(b)).

Our contributions are summarized as follows:

- We propose MeDUET, which, to the best of our knowledge, is the first unified pretraining framework in medical imaging that supports both synthesis and analysis.
- To bridge the gap in medical imaging, we propose a novel SSL paradigm within the VAE latent space, employing a disentanglement formulation that aligns the objectives of synthesis and analysis, reinforced by a demixing objective that encourages factor separation identifiable.
- We design two factor-aware pretext tasks, MFTD and SiQC, which target mixed-token inference and swap-invariant contrast within the factor spaces, respectively, jointly optimizing these complementary objectives.
- Comprehensive evaluation demonstrates the superior performance of MeDUET in both downstream synthesis and analysis tasks across 5 datasets, 4 tasks and 2 modalities. For synthesis, it yields substantial improvements over baseline methods in generation fidelity, diversity, convergence speed, and controllability, while for analysis, it exhibits strong domain generalization and remarkable data efficiency.

2. Related Work

3D Medical Image Synthesis. 3D medical image synthesis aims to produce synthetic volumetric data for various clinical applications [75, 93]. Advances in natural-image diffusion have accelerated progress in this area [10, 36], with multiple works showing high-fidelity 3D generations

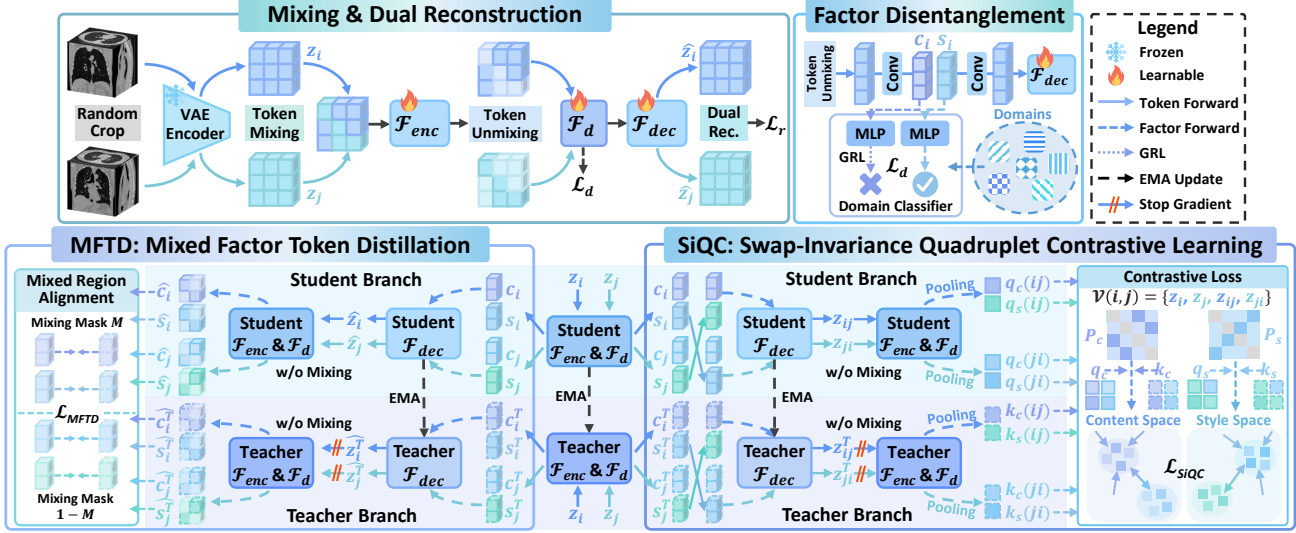


Figure 3. **The overall framework of our MeDUET:** (a) *Mixing & Dual Reconstruction* aims to perform demixing between two mixed patch tokens. (b) *Factor Disentanglement* module explicitly decomposes encoded latent patches into content and style representations, using a domain classifier to empower them as domain-invariant and domain-identifiable, respectively. (c) *MFTD* performs knowledge distillation on the mixed regions within the factor space. (d) *SiQC* enforces contrastive consistency within the factor space, encouraging invariance to the swapped factor while preserving the discriminability of the retained one.

capturing intricate structures and realistic details [24, 56]. Diffusion models have also been applied to diverse clinical tasks, including data augmentation [69], CT reconstruction [15], and counterfactual generation [88]. In this work, we propose initializing diffusion models with pre-trained SSL models in the VAE latent space, which not only accelerates convergence but also improves synthesis quality. Moreover, the content and style factors encoded by the disentangled representation learning in MeDUET enable promising controllability in generation.

3D Medical Image Analysis. Given the scarcity of labeled data in medical imaging, pretraining SSL on large unlabeled 3D data has become a strong paradigm for medical image analysis [13, 39]. Most methods follow contrastive learning (CL) [30, 79] or masked image modeling (MIM) [72, 96]. Previous CL-based approaches rely on strong volumetric augmentations [61], while mask or remove 3D patches and learn to reconstruct them [65]. However, existing methods tend to overemphasize scanner appearance, entangling content and style [2, 57, 65], which hinders their performance in cross-domain and low-data settings. In contrast, our method employs explicit factor disentanglement to learn robust and domain-consistent semantics, thus improving out-of-distribution performance and data efficiency.

Diffusion Models for Representation Learning. Given the competitive performance of diffusion models in various generation tasks, recent studies have emerged to explore their representational capabilities [14, 35, 78], demonstrating that diffusion models can serve as effective visual learners [51, 71]. Other approaches modify diffusion architec-

tures to learn discriminative representations for visual perception tasks [12, 58, 82]. However, large-scale applications in medical imaging remain underexplored.

Disentangled Representation Learning. Disentangled representation learning aims to train models that can separate interpretable and informative factors hidden in observed data [32, 45, 73]. Prior works focus on augmenting generative models to enhance their disentanglement capability [41, 86]. In medical imaging, typical applications include disease decomposition [66], harmonization [81], controllable generation [8, 50, 52], and domain generalization [23, 85]. In this paper, our MeDUET is inspired by recent trends of decomposing input volumes into domain-invariant content and domain-specific style [6, 23, 52].

3. Method

The overall framework of MeDUET is presented in Fig. 3, which is based on the VAE latent space, disentangling content from style and using token demixing as supervision. A student-teacher design supports two auxiliary proxy tasks, MFTD and SiQC, which provide targeted guidance to mixed tokens and enforce swap-invariant structure.

3.1. Demixing & Dual Reconstruction

To turn multi-center heterogeneity into an explicit supervisory signal and make factor disentanglement practically identifiable, we introduce a token demixing module that constructs and inverts controlled factor mixtures, which are consistent with real clinical shifts. Specifically, given an

input volume, we first obtain its latent representation via the frozen VAE tokenizer, and all subsequent operations are performed in latent space during pretraining. Two sets of latent volume patches $\{\mathbf{z}_i, \mathbf{z}_j\}$ are sampled from two random volumes within a batch. Following the MIM paradigm, we then generate a mixed patch using a mixing function ϕ_m that combines the corresponding visible cubic tokens from \mathbf{z}_i and \mathbf{z}_j according to a binary mask M [9, 43]. Then the ViT encoder \mathcal{F}_{enc} takes the mixed tokens as input for representation learning. An unmixing function ϕ_u restores tokens to their original spatial positions based on the mixing notation M . The factor disentanglement module \mathcal{F}_d is then applied, while the lightweight decoder \mathcal{F}_{dec} reconstructs the original volumetric patches $\{\hat{\mathbf{z}}_i, \hat{\mathbf{z}}_j\}$ from the visible tokens. Finally, the dual reconstruction loss is formulated as

$$\mathcal{L}_r = \|\hat{\mathbf{z}}_i - \mathbf{z}_i\|_2^2 + \|\hat{\mathbf{z}}_j - \mathbf{z}_j\|_2^2. \quad (1)$$

3.2. Factor Disentanglement

The factor disentanglement module \mathcal{F}_d decomposes the encoder output into two factors that serve complementary purposes: a domain-invariant content representation $\mathbf{c}_i \in \mathbb{R}^{L \times D_c}$ and a domain-specific style representation $\mathbf{s}_i \in \mathbb{R}^{L \times D_s}$, where L is the token length. We implement \mathcal{F}_d with a lightweight convolutional layer.

Domain Classifier. To further reinforce disentanglement, we introduce domain classifiers to both factor learning process. The content branch is trained in an adversarial manner via a gradient-reversal layer (GRL) [19] so that the encoder removes domain shift information from \mathbf{c}_i , whereas the style branch is trained normally to make \mathbf{s}_i distinguishable of the domain. Specifically, each branch uses a three-layer MLP domain classifier with a cross-entropy loss:

$$\mathcal{L}_d(i) = -\log([\sigma(\mathcal{G}_c(\mathcal{R}(\bar{\mathbf{c}}_i)))]_{y_i}) - \log([\sigma(\mathcal{G}_s(\bar{\mathbf{s}}_i)))]_{y'_i}, \quad (2)$$

where y_i is the domain label, $\bar{\mathbf{c}}_i$ and $\bar{\mathbf{s}}_i$ denote the factor vectors after token-level pooling, \mathcal{G}_c and \mathcal{G}_s are domain classifiers for content and style disentanglement modules, respectively, \mathcal{R} represents the GRL, and σ denotes the softmax function. We perform the same operation on \mathbf{z}_j , yielding $\mathcal{L}_d(j)$. The overall domain classifier loss is expressed as

$$\mathcal{L}_d = \mathcal{L}_d(i) + \mathcal{L}_d(j). \quad (3)$$

Then the two factor tokens are integrated via another convolutional layer to obtain aggregated tokens for subsequent reconstruction process.

3.3. MFTD

Intuitively, token mixing introduces information loss, leaving mixed regions ambiguous and thereby weakening the constraints on the factor space. To this end, we devise MFTD, which provides factor-specific teacher supervision by distilling content from the content source and

style from the style source to prevent factor leakage, enforce invariance under incomplete contextual information, and strengthen disentanglement through fine-grained factor-level rather than coarse patch-level alignment.

Concretely, given the recovered patch tokens $\hat{\mathbf{z}}_i$ and $\hat{\mathbf{z}}_j$, we re-encode them by feeding them into \mathcal{F}_{enc} and \mathcal{F}_d again without mixing, yielding novel factor tokens $\{\hat{\mathbf{c}}_i, \hat{\mathbf{s}}_i\}$ and $\{\hat{\mathbf{c}}_j, \hat{\mathbf{s}}_j\}$, which denote the full patch factors. Additionally, we introduce a teacher model, which is updated via the Exponential Moving Average (EMA). For the MFTD teacher network, we obtain $\{\hat{\mathbf{c}}_i^T, \hat{\mathbf{s}}_i^T\}$ and $\{\hat{\mathbf{c}}_j^T, \hat{\mathbf{s}}_j^T\}$ through an identical re-encoding and re-disentanglement process performed by the teacher model, which provides global contextual priors to guide the student model. The objective functions are designed to minimize the discrepancy between the teacher and student factor outputs in the mixed regions:

$$\Delta_i^c = \frac{1}{D_c} \|\hat{\mathbf{c}}_i - \text{sg}[\hat{\mathbf{c}}_i^T]\|_2^2, \quad \Delta_j^c = \frac{1}{D_c} \|\hat{\mathbf{c}}_j - \text{sg}[\hat{\mathbf{c}}_j^T]\|_2^2, \quad (4)$$

$$\mathcal{L}_{\text{MFTD}}^c = \frac{\|\Delta_i^c \odot M + \Delta_j^c \odot (1 - M)\|_1}{L}, \quad (5)$$

where $\text{sg}[\cdot]$ denotes the stop gradient operation. Notably, the token distances are calculated by averaging across dimensions to mitigate the influence of high-dimensional factor representations. By combining it with the similarly computed loss of style tokens, the total token distillation loss is defined as the weighted sum:

$$\mathcal{L}_{\text{MFTD}} = \lambda_c \mathcal{L}_{\text{MFTD}}^c + \mathcal{L}_{\text{MFTD}}^s. \quad (6)$$

3.4. SiQC

Mixing yields paired views that share either content or style. To make disentanglement effective in practice, a specialized objective is required to (i) pull together views sharing the same content while remaining sensitive to style, and (ii) symmetrically, pull together views sharing the same style while remaining sensitive to content, which generic contrastive objectives fail to enforce. To this end, SiQC employs a swap-invariant quadruplet objective that pulls together same-content (different-style) and same-style (different-content) pairs while pushing apart cross-factor negatives, thus explicitly structuring both factor spaces.

Content-style swapping. Given the learned factors, we exchange factors between two input volumes, producing $\{\mathbf{c}_i, \mathbf{s}_j\}$ and $\{\mathbf{c}_j, \mathbf{s}_i\}$, which are then fed into \mathcal{F}_{dec} to generate recovered patches \mathbf{z}_{ij} and \mathbf{z}_{ji} , respectively. Next, \mathcal{F}_{enc} and \mathcal{F}_d are utilized again for re-encoding without mixing operation, yielding $\{\mathbf{c}_{ij}, \mathbf{s}_{ij}\}$ and $\{\mathbf{c}_{ji}, \mathbf{s}_{ji}\}$. The former retains the anatomical structure information of \mathbf{z}_i and domain style characteristics of \mathbf{z}_j , while the latter does the opposite.

Quadruplet construction. Let the two inputs be \mathbf{z}_i and \mathbf{z}_j , we form the quadruplet $\mathcal{V}(i, j) = \{\mathbf{z}_i, \mathbf{z}_j, \mathbf{z}_{ij}, \mathbf{z}_{ji}\}$. Taking the content space contrastive learning as an example, $\mathbf{q}_c(a)$

and $\mathbf{k}_c(b)$ are defined as the pooled and L2-normalized student/teacher content features for view $a, b \in \mathcal{V}(i, j)$.

Contrastive loss. Drawing inspiration from [40], we define the binary positive mask as

$$\delta_c(\mathbf{z}_i) = \delta_c(\mathbf{z}_{ij}) = i, \quad \delta_c(\mathbf{z}_j) = \delta_c(\mathbf{z}_{ji}) = j, \quad (7)$$

$$P_c(a, b) = \mathbf{1}\{\delta_c(a) = \delta_c(b)\} \cdot \mathbf{1}\{a \neq b\}, \quad (8)$$

where $\delta_c(\cdot)$ is the content identity map, and $\mathbf{1}$ is the indicator function. Then the similarity and loss are defined as

$$S_c(a, b) = \exp(\alpha_c) \mathbf{q}_c(a) \cdot \text{sg}[\mathbf{k}_c^T(b)], \quad S_c(a, a) = -\infty, \quad (9)$$

$$\ell_c(a, b) = S_c(a, b) - \log \sum_{b' \in \mathcal{V}(i, j) \setminus \{a\}} \exp(S_c(a, b')), \quad (10)$$

$$\mathcal{L}_{\text{SiQC}}^c = \mathbb{E}_{a \in \mathcal{V}(i, j)} \left[-\frac{\sum_{b \in \mathcal{V}(i, j)} P_c(a, b) \ell_c(a, b)}{\sum_{b \in \mathcal{V}(i, j)} P_c(a, b)} \right], \quad (11)$$

$$\mathcal{L}_{\text{SiQC}} = \mathcal{L}_{\text{SiQC}}^c + \mathcal{L}_{\text{SiQC}}^s. \quad (12)$$

where α_c is a learnable scale. This objective pulls the positive pairs $\{\mathbf{z}_i, \mathbf{z}_{ij}\}$ and $\{\mathbf{z}_j, \mathbf{z}_{ji}\}$ together in content space while pushing apart all other pairs. During SiQC, teacher features are stop-grad, while student features and the student path that produces swapped views remain fully differentiable, so that SiQC improves both factor encoders and the swap mechanism.

The total loss of MeDUET pretraining is formulated as

$$\mathcal{L} = \mathcal{L}_r + \lambda_1 \mathcal{L}_d + \lambda_2 \mathcal{L}_{\text{MFTD}} + \lambda_3 \mathcal{L}_{\text{SiQC}}. \quad (13)$$

where λ_i are coefficients to balance loss contribution.

3.5. Initialization for Downstream Applications

For downstream generative tasks, we carefully modify the pretrained ViT model to adapt and initialize the DiT/SiT [49, 55] models for diffusion-based generation. Following [14], we reintroduce the shift (β) and scale (γ) parameters to implement AdaLN-Zero and layer normalization blocks as conditional input modules. For analysis tasks, we adopt UNETR [27] as the backbone, which seamlessly inherits the pretrained ViT weights from MeDUET. To address inconsistencies in positional embeddings, trilinear interpolation is applied to upscale them, ensuring consistency between the patch sizes used during pretraining and those in the downstream phases.

4. Experiments

4.1. Experimental Setup

Datasets. To ensure a fair comparison with previous works, we employ the VoCo-10k dataset [79, 80] for pretraining, which includes 10 public CT datasets covering diverse sources and anatomical regions [1, 16, 22, 42, 48, 59, 62,

Table 1. **Synthesis performance comparison.** The best results are **bolded**, and the second best results are underlined. †: using pre-defined metadata vectors. ‡: using learned content and style vectors. 100k/200k: pretrained steps of MeDUET. We evaluate SiT B/4 + MeDUET for subsequent experiments, using pretraining weights from 200k steps by default.

Method	FID ↓	MMD ↓	MS-SSIM ↓
<i>Medical Image Synthesis Models</i>			
WDM [18]	0.9668	0.6612	0.2284
MedSyn [84]	0.9873	0.6734	0.2325
MAISI [24]	0.9139	0.6292	0.2057
3D MedDiffusion [69]	0.9216	0.6327	0.2032
<i>General Diffusion Models</i>			
DiT-B/4†	0.9207	0.6329	0.1957
DiT-B/4‡	0.9074	0.6175	0.1906
MeDUET 100k/200k†	0.8763 / 0.8727	0.6097 / 0.6074	0.1892 / 0.1876
MeDUET 100k/200k‡	0.8642 / 0.8611	0.6028 / 0.6003	0.1824 / 0.1803
SiT-B/4†	0.8670	0.6023	0.1834
SiT-B/4‡	0.8533	0.6012	0.1798
MeDUET 100k/200k†	0.8039 / 0.8011	0.5806 / 0.5782	0.1712 / 0.1692
MeDUET 100k/200k‡	0.7908 / 0.7874	0.5627 / 0.5598	0.1677 / 0.1659

63, 77, 97], consisting of 10,500 CT scans in total. For downstream experiments, all diffusion models are trained using the VoCo-10k dataset. Additionally, we conduct analysis experiments on five public datasets: BTCV [42], WORD [47], AMOS [38] and BraTS 21 [3] for segmentation tasks, and CC-CCII [91] for the COVID-19 classification task. We use consistent dataset settings as previous works [65, 79, 95, 96]. Further details of the datasets can be found in the supplementary materials.

Implementation Details. We employ MAISI-VAE [24] as the tokenizer to generate latent representations of the input volumes, which are cached to facilitate efficient training and inference. The pretraining process consists of 200k steps, using the AdamW [46] optimizer with a cosine learning rate schedule. The isotropic voxel spacing is set to 1.5 mm, and each subvolume patch has a size of $96 \times 96 \times 96$. We introduce the MFTD module at 40k steps when the teacher model has been updated stably. We treat each dataset as a domain because it typically reflects a distinct center/protocol/scanner and thus serves as a stable proxy for style shifts. We generate content and style vectors for entire volumes using the pretrained MeDUET weights. For synthesis, we condition DiT/SiT on the content and style, replacing coarse metadata with fine-grained control. For analysis, we use the style vector to drive label-preserving style augmentation. Additional implementation details are provided in the supplementary materials.

4.2. Medical Image Synthesis

We compare MeDUET with SOTA 3D medical image synthesis methods [18, 24, 69, 84]. Furthermore, we integrate our pretrained model into two diffusion transformers: DiT [55] and SiT [49], which we follow the training settings by default. We reimplemented all baseline methods from scratch using the pretraining dataset. Notably, we lever-

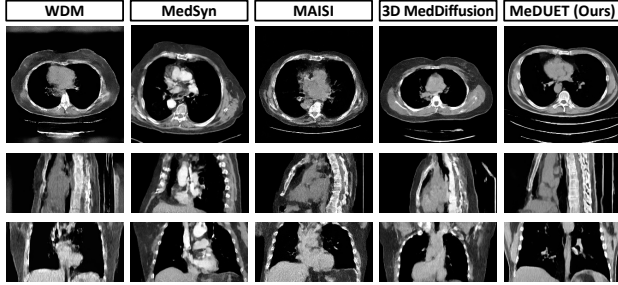


Figure 4. **Qualitative comparison** of synthesized volumes.

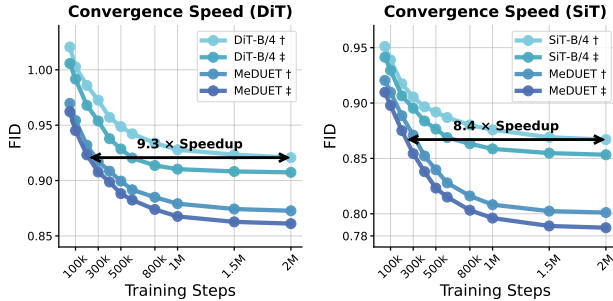


Figure 5. **Convergence speed comparison.** Left: Convergence acceleration for DiT. Right: Convergence acceleration for SiT. †: using pre-defined metadata. ‡: using learned content and style.

age the learned content and style vectors as condition with classifier-free guidance (CFG) [33] instead of pre-defined metadata vectors (e.g. body region, voxel spacing). Evaluations are conducted on the generated 1k volumes. For evaluation metrics, following [69], Fréchet Inception Distance (FID) [31] and Maximum Mean Discrepancy (MMD) [21] are used to assess the fidelity and realism of the synthetic images, while Multi-Scale Structural Similarity Index (MS-SSIM) [76] is employed to evaluate the diversity. For FID and MMD evaluation, we use the MedicalNet 3D [11] as the feature extractor to compute whole-volume 3D features per scan.

Synthesis Quality Comparison. We exclude any improvements to DiT and SiT, such as architectural modifications [20, 94] and acceleration techniques [87, 89], which are not line with our core objective. From Table 1, MeDUET achieves SOTA performance across all three metrics, with FID scores of 0.7874 and 0.8611 for SiT and DiT, respectively, and achieves lower MMD and MS-SSIM values than all baselines, indicating superior anatomical fidelity and appearance diversity. The learned disentangled factors consistently outperform the previously used metadata vectors, emphasizing the effectiveness of our disentangled factor learning. Fig. 4 presents a visual comparison of images synthesized by our method and baselines.

Convergence Acceleration. Fig. 5 displays the training progress for DiT, SiT, and MeDUET. With MeDUET initialization, DiT achieves a **9.3 ×** faster FID convergence speed and SiT achieves an **8.4 ×** speedup. The gains grow

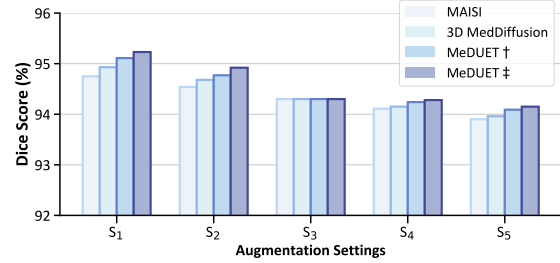


Figure 6. Performance comparison of **data augmentation**. †: using pre-defined metadata vectors. ‡: using learned content and style vectors. S_1 : 100% synthetic data. S_2 : 50% real data and 50% synthetic data. S_3 : 100% real data. S_4 : 100% real data and 50% synthetic data. S_5 : 100% real data and 100% synthetic data.

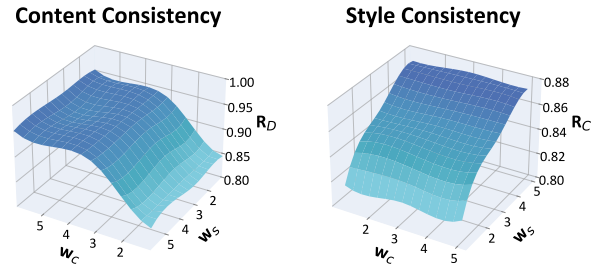


Figure 7. **Content and style consistency surface.** w_c, w_s : CFG scales for content and style. R_D : Dice ratio between the segmentations of the reference and the generated volumes; a higher value indicates greater anatomical similarity and thus higher content consistency. R_C : Hit rate of the style classifier on the generated volumes; a higher value reflects greater style similarity, i.e., higher style consistency.

with learned factor and longer pretraining, confirming the effectiveness of our disentanglement and initialization.

Conditional Generation for Data Augmentation. Following [24, 69], we integrate ControlNet [64, 92] and condition the diffusion model on segmentation masks to improve controllability. Subsequently, the synthesized volumes are employed as augmented data to enhance segmentation performance. We train nnU-Net [37] on TotalSegmentator [77] under five training regimes. As illustrated in Fig. 6, our MeDUET-guided, controllable synthesis consistently surpasses baselines across the five augmentation settings. Disentangled factors further boost segmentation, indicating anatomy-preserving content control and style-aware diversification, and validating our disentangled, controllable generation framework.

Content and Style Consistency. To assess controllable generation without manual latent edits, we use dual-conditional CFG [33], independently scaling content w_c and style w_s during sampling. For content consistency, we fix TotalSegmentator [77] content references, sample styles from other domains, sweep (w_c, w_s) , and compute the Dice ratio R_D between segmentations of the references and the

Table 2. Results on the **segmentation task** under different data proportions. The third row denotes the data ratios for training. We report the mean Dice score (%). The best results are **bolded**, and the second best results are underlined.

Method	Dice Score (%) \uparrow																			
	BTCV					AMOS					WORD					BraTS 21				
	1-shot	10%	50%	100%	Avg	1-shot	10%	50%	100%	Avg	1-shot	10%	50%	100%	Avg	1-shot	10%	50%	100%	Avg
<i>From Scratch</i>																				
UNETR [27]	68.19	78.30	87.28	92.33	81.53	60.29	86.82	93.54	94.62	83.82	62.48	90.76	92.87	94.03	85.03	51.91	77.41	84.56	85.24	74.78
Swin UNETR [26]	71.28	78.54	88.06	92.65	82.63	63.18	87.26	93.80	95.29	84.88	64.39	91.05	92.93	94.01	85.59	55.82	79.56	85.42	86.15	76.74
<i>General SSL</i>																				
MAE3D [13]	65.95	76.71	85.81	91.28	79.94	57.39	85.27	92.63	94.25	82.38	58.96	90.24	92.68	94.06	83.98	54.57	78.86	85.29	86.19	76.23
SimMIM [83]	65.42	76.08	84.93	90.89	79.33	57.82	85.06	92.48	93.94	82.33	57.75	90.05	92.51	93.81	83.53	52.39	77.63	85.12	85.54	75.17
MoCo v3 [28]	66.49	77.86	86.57	91.83	80.69	59.60	86.29	93.37	94.67	83.48	57.83	90.22	92.46	93.92	83.61	52.20	77.72	85.24	85.76	75.23
<i>Medical Image SSL</i>																				
Swin UNETR [26]	72.87	80.42	89.93	92.96	84.05	63.01	89.75	93.52	94.69	85.24	66.85	91.13	93.26	94.03	86.32	56.93	79.70	85.58	86.62	77.21
SwinMM [74]	72.28	81.97	91.36	93.58	84.80	63.56	89.24	93.75	94.84	85.35	74.65	91.39	93.48	94.19	88.43	57.12	79.51	85.40	86.73	77.19
GVSL [30]	<u>74.92</u>	83.75	<u>91.41</u>	93.43	<u>85.88</u>	<u>63.70</u>	89.72	93.68	94.97	85.52	76.92	91.30	93.39	94.12	88.93	54.79	80.20	85.61	86.92	76.88
VoCo [79]	73.27	<u>84.15</u>	90.20	<u>93.62</u>	85.31	62.75	89.84	94.07	95.37	85.51	70.90	91.47	93.51	94.24	87.53	<u>57.30</u>	<u>80.71</u>	<u>85.77</u>	87.09	<u>77.72</u>
GL-MAE [95]	69.29	79.63	89.61	93.07	82.90	61.93	87.52	93.70	95.14	84.57	65.93	91.66	93.13	94.16	86.22	54.98	79.38	84.42	86.75	76.38
MIM [96]	71.86	81.05	90.23	93.14	84.07	61.84	88.68	94.05	95.03	84.90	71.49	91.91	93.30	94.02	87.68	56.36	79.06	84.82	86.84	76.77
Hi-End-MAE [65]	72.45	83.02	90.80	93.19	84.86	63.23	<u>90.03</u>	<u>94.16</u>	95.76	<u>85.80</u>	<u>77.24</u>	<u>92.24</u>	<u>93.65</u>	94.34	<u>89.37</u>	54.46	80.23	85.71	<u>87.33</u>	76.93
MeDUET	78.72	87.04	92.24	94.06	88.02	65.18	90.36	94.34	<u>95.48</u>	86.34	79.56	92.61	93.83	<u>94.28</u>	90.07	58.05	80.83	85.82	87.39	78.02

Table 3. Results on the **classification task** on the CC-CCII dataset under different data proportions. The second row denotes the data ratios for training. We report the Accuracy (%).

Method	Accuracy (%) \uparrow			
	10%	50%	100%	Avg
<i>From Scratch</i>				
UNETR [27]	73.80	82.40	88.65	81.62
Swin UNETR [26]	77.01	86.62	88.32	83.98
<i>Medical Image SSL</i>				
Swin-UNETR [26]	77.64	87.33	89.42	84.80
SwinMM [74]	81.49	91.27	92.23	88.33
GVSL [30]	86.16	91.08	93.26	90.17
VoCo [79]	<u>86.85</u>	91.86	<u>93.45</u>	<u>90.72</u>
GL-MAE [95]	80.63	88.62	92.13	87.13
MIM [96]	82.57	89.74	92.75	88.35
Hi-End-MAE [65]	78.76	88.15	92.59	86.50
MeDUET	88.68	<u>91.79</u>	93.59	91.35

generated volumes. For style consistency, we fix style references and report the style-classifier hit rate R_C and its monotonicity with w_s . We use nnU-Net [37] as the segmenter and MeDUET’s domain classifier as the style classifier. As shown in Fig. 7, R_D increases with w_c and quickly saturates near 1 across w_s , while R_C rises strictly with w_s and is insensitive to w_c . Thus, content tokens remain geometrically stable and style tokens control appearance, demonstrating MeDUET’s impressive controllability.

4.3. Medical Image Analysis

We validate MeDUET with both General [13, 28, 29, 83] and Medical SSL [26, 27, 30, 65, 74, 79, 95, 96] on analysis tasks for a thorough comparison. The experimental results are reported using official pretrained model weights for Medical SSL methods.

Superior Performance for Cross-Domains and Data Efficiency. We fine-tune pretrained models for segmentation tasks on four datasets with varying proportions of labeled data, and the results are summarized in Table 2. AMOS and WORD correspond to unseen domains during pretraining,

Table 4. **Synthesis performance comparison with 3D medical image SSL in the latent space.** †: using pre-defined metadata vectors. ‡: using learned content and style vectors.

Method	FID \downarrow	MMD \downarrow	MS-SSIM \downarrow
SiT-B/4 + MAE3D† [13]	0.8416	0.5972	0.1871
SiT-B/4 + MAE3D‡ [13]	0.8265 (-0.0151)	0.5816 (-0.0156)	0.1796 (-0.0075)
SiT-B/4 + GL-MAE† [95]	0.8322	0.5947	0.1803
SiT-B/4 + GL-MAE‡ [95]	0.8147 (-0.0175)	0.5803 (-0.0144)	0.1762 (-0.041)
SiT-B/4 + Hi-End-MAE† [65]	0.8189	0.5846	0.1773
SiT-B/4 + Hi-End-MAE‡ [65]	0.8094 (-0.0095)	0.5785 (-0.0061)	0.1736 (-0.0037)
SiT-B/4 + MeDUET†	<u>0.8011</u>	<u>0.5782</u>	<u>0.1692</u>
SiT-B/4 + MeDUET‡	0.7874 (-0.0137)	0.5598 (-0.0184)	0.1659 (-0.0033)

while BraTS 21 represents an unseen modality (from CT to MRI). MeDUET consistently improves Dice across domains and label ratios, while prior methods are less stable and underperform with unseen domains or limited labels. The robustness and data efficiency of MeDUET can be attributed to its strong capability to learn invariant anatomical representations that are robust to domain variations.

Remarkable One-shot Segmentation Performance.

From Table 2, under the one-shot segmentation setting, MeDUET surpasses the strongest SSL baseline by an average of 2.09% Dice Scores across four 3D medical benchmarks. These results suggest that the factor disentanglement and demixing mechanism in MeDUET enables more label-efficient representations.

Strong Generalization Capability for MRI data.

As shown in Table 2, MeDUET outperforms existing SOTA methods on the BraTS 21 dataset under various data proportions, demonstrating the promising generalization ability of our MeDUET for unseen modalities.

Classification Tasks.

From Table 3, our MeDUET yields outperformance over SOTA baselines for the classification task on the CC-CCII dataset, which achieves a 0.63% improvement of accuracy in average under various data ratios.

Table 5. **Ablation results** on loss functions and model components. w/o Disent.: Factor disentanglement is removed by excluding \mathcal{L}_d and $\mathcal{L}_{\text{SIQC}}$, and MFTD is modified to perform token-level distillation. w/o Demix.: The demixing module is disabled, resulting in a vanilla masked reconstruction paradigm.

Method	Synthesis			Analysis			
	FID ↓	MMD ↓	MS-SSIM ↓	Dice Score (%) ↑			
				BTCV		WORD	
			1-shot	100%	1-shot	100%	
<i>Loss Functions</i>							
w/o \mathcal{L}_d	0.8147	0.5836	0.1758	73.86	93.34	72.18	94.14
w/o $\mathcal{L}_{\text{MFTD}}$	0.7916	0.5623	0.1689	77.43	93.81	78.62	94.17
w/o $\mathcal{L}_{\text{SIQC}}$	0.7929	0.5619	0.1696	77.94	93.78	79.30	94.21
<i>Components</i>							
w/o Disent.	0.8460	0.5924	0.1802	71.63	93.28	70.41	94.06
w/o Demix.	0.7962	0.5677	0.1713	78.09	93.92	79.27	94.19
MeDUET	0.7874	0.5598	0.1659	78.72	94.06	79.56	94.28

Table 6. **Linear probe** classification results of learned content and style codes. We report the Accuracy (%) and AUC (%).

Method	Content		Style	
	Accuracy (%) ↓	AUC (%) ↓	Accuracy (%) ↑	AUC (%) ↑
w/o \mathcal{L}_d	57.53	75.48	51.46	71.52
w/o $\mathcal{L}_{\text{MFTD}}$	24.20	63.21	96.07	93.11
w/o $\mathcal{L}_{\text{SIQC}}$	28.77	68.98	92.04	90.23
w/o Demix.	23.95	62.92	96.18	93.26
MeDUET	23.59	61.56	96.43	93.59

4.4. Medical SSL for Generative Transfer

To isolate the contribution of our disentangling objectives, we reimplement representative 3D ViT-based medical SSL [13, 65, 95] within the same VAE latent space and transfer their encoders to initialize SiT. Under matched experimental protocols, we compare their synthesis quality, as reported in Table 4. As shown, MeDUET surpasses baselines transferred within the identical latent space. Furthermore, the introduction of our disentangled factors leads to varying degrees of improvement for latent medical SSL. Crucially, with setups all held fixed, the consistent gains across three metrics isolate the benefit of our disentangling components rather than model capacity or data advantages. Taken together, these results establish MeDUET as a more transferable and effective pretraining paradigm for 3D medical imaging than latent-space SSL alone.

4.5. Ablation Study

Loss Functions and Components. From Table 5, removing any single loss consistently worsens synthesis, and disabling disentanglement leads to the largest few-shot Dice drop. With all components enabled, MeDUET achieves the best synthesis and highest segmentation Dice, indicating these components are complementary and essential for both generative quality and segmentation generalization.

Factor Identifiability. In this section, we analyze the effectiveness of disentanglement both quantitatively and qual-

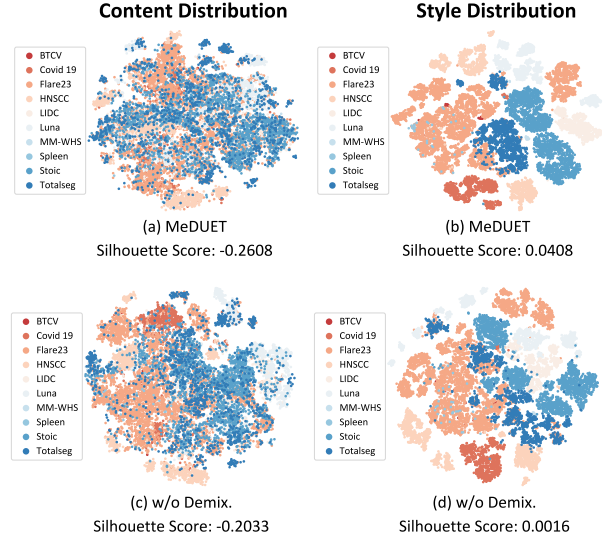


Figure 8. The **t-SNE visualization** of MeDUET content and style codes, where points are color-coded according to their domain labels. Left: Content distribution. Right: Style distribution.

itatively by investigating factor identifiability empirically: the content vector should be domain-invariant and sufficient for downstream tasks, while the style vector should be domain-specific and task-independent. We first conduct linear-probe classification experiments using the learned factors as input and domain categories as labels. As reported in Table 6, the linear probe trained on style vectors achieves high domain sensitivity than variants, confirming that the style branch effectively captures more protocol-specific cues. Conversely, the probe trained on content vectors yields lower domain discriminative that is approximately random classification, indicating lower domain leakage and more effective factor disentanglement.

In addition, we visualize the t-SNE of factor codes learned by MeDUET and its variant w/o Demix. As shown in Fig. 8, the content vectors learned by MeDUET exhibit an entangled and interspersed distribution across domain labels, with a lower silhouette score than the variant w/o Demix., verifying its ability to extract domain-invariant knowledge. In contrast, the style representations display better domain alignment, with clear and distinct boundaries and a higher silhouette score, indicating their capability to capture domain-specific information. These results further justify the rationale behind our demixing module, which facilitates more disentangled and identifiable factor learning.

5. Conclusion

In this work, we present MeDUET, a unified pretraining framework for 3D medical imaging that learns identifiable content-style factors within a VAE latent space and transfers seamlessly to both generative and analytical

tasks. Our design explicitly enforces disentanglement so that content governs anatomical structure while style captures domain attributes. Extensive experiments demonstrate that MeDUET achieves superior performance for versatile synthesis and analysis applications. By unleashing the potential of SSL for both medical image generation and understanding, we believe MeDUET provides valuable insights that can guide future research on pretraining strategies for 3D medical imaging.

References

- [1] Samuel G. Armato III, Geoffrey McLennan, Luc Bidaut, Michael F. McNitt-Gray, Charles R. Meyer, Anthony P. Reeves, Binsheng Zhao, Denise R. Aberle, Claudia I. Henschke, Eric A. Hoffman, Ella A. Kazerooni, Heber MacMahon, Edwin J. R. van Beek, David Yankelevitz, Alberto M. Biancardi, Peyton H. Bland, Matthew S. Brown, Roger M. Engelmann, Gary E. Laderach, Daniel Max, Richard C. Pais, David P.-Y. Qing, Rachael Y. Roberts, Amanda R. Smith, Adam Starkey, Poonam Batra, Philip Caligiuri, Ali Farooqi, Gregory W. Gladish, C. Matilda Jude, Reginald F. Munden, Iva Petkowska, Leslie E. Quint, Lawrence H. Schwartz, Baskaran Sundaram, Lori E. Dodd, Charles Fenimore, David Gur, Nicholas Petrick, John Freymann, Justin Kirby, Brian Hughes, Alessi Vande Castele, Sangeeta Gupte, Maha Sallam, Michael D. Heath, Michael H. Kuhn, Ekta Dharaiya, Richard Burns, David S. Fryd, Marcos Salganicoff, Vikram Anand, Uri Shreter, Stephen Vastagh, Barbara Y. Croft, and Laurence P. Clarke. The lung image database consortium (lidc) and image database resource initiative (idri): A completed reference database of lung nodules on ct scans. *Medical Physics*, 38(2):915–931, 2011. [5](#), [1](#), [2](#)
- [2] Mahmoud Assran, Mathilde Caron, Ishan Misra, Piotr Bojanowski, Florian Bordes, Pascal Vincent, Armand Joulin, Mike Rabbat, and Nicolas Ballas. Masked siamese networks for label-efficient learning. In *European conference on computer vision*, pages 456–473, 2022. [3](#)
- [3] Ujjwal Baid, Satyam Ghodasara, Suyash Mohan, Michel Bilello, Evan Calabrese, Errol Colak, Keyvan Farahani, Jayashree Kalpathy-Cramer, Felipe C Kitamura, Sarthak Pati, et al. The rsna-asnr-miccai brats 2021 benchmark on brain tumor segmentation and radiogenomic classification. *arXiv preprint arXiv:2107.02314*, 2021. [5](#), [2](#)
- [4] Qi Bi, Jingjun Yi, Hao Zheng, Wei Ji, Yawen Huang, Yuxiang Li, and Yefeng Zheng. Learning generalized medical image representation by decoupled feature queries. *IEEE Transactions on Pattern Analysis and Machine Intelligence*, pages 1–18, 2025. [1](#), [2](#)
- [5] Manh-Ha Bui, Toan Tran, Anh Tran, and Dinh Phung. Exploiting domain-specific features to enhance domain generalization. In *Advances in Neural Information Processing Systems*, pages 21189–21201, 2021. [2](#)
- [6] Zhuotong Cai, Jingmin Xin, Chenyu You, Peiwen Shi, Siyuan Dong, Nicha C. Dvornek, Nanning Zheng, and James S. Duncan. Style mixup enhanced disentanglement learning for unsupervised domain adaptation in medical image segmentation. *Medical Image Analysis*, 101:103440, 2025. [3](#)
- [7] Mathilde Caron, Hugo Touvron, Ishan Misra, Hervé Jégou, Julien Mairal, Piotr Bojanowski, and Armand Joulin. Emerging properties in self-supervised vision transformers. In *Proceedings of the IEEE/CVF International Conference on Computer Vision (ICCV)*, pages 9650–9660, 2021. [1](#)
- [8] Zengyang Che, Zheng Zhang, Yaping Wu, and Meiyun Wang. Disentangle and then fuse: A cross-modal network for synthesizing gadolinium-enhanced brain mr images. *IEEE Transactions on Circuits and Systems for Video Technology*, 35(6):6021–6033, 2025. [3](#)
- [9] Kai Chen, Zhili Liu, Lanqing Hong, Hang Xu, Zhen-guo Li, and Dit-Yan Yeung. Mixed autoencoder for self-supervised visual representation learning. In *Proceedings of the IEEE/CVF Conference on Computer Vision and Pattern Recognition (CVPR)*, pages 22742–22751, 2023. [4](#)
- [10] Qi Chen, Xiaoxi Chen, Haorui Song, Zhiwei Xiong, Alan Yuille, Chen Wei, and Zongwei Zhou. Towards generalizable tumor synthesis. In *Proceedings of the IEEE/CVF Conference on Computer Vision and Pattern Recognition (CVPR)*, pages 11147–11158, 2024. [2](#)
- [11] Sihong Chen, Kai Ma, and Yefeng Zheng. Med3d: Transfer learning for 3d medical image analysis. *arXiv preprint arXiv:1904.00625*, 2019. [6](#)
- [12] Xinlei Chen, Zhuang Liu, Saining Xie, and Kaiming He. Deconstructing denoising diffusion models for self-supervised learning. In *The Thirteenth International Conference on Learning Representations*, 2025. [3](#)
- [13] Zekai Chen, Devansh Agarwal, Kshitij Aggarwal, Wiem Safta, Mariann Micsinai Balan, and Kevin Brown. Masked image modeling advances 3d medical image analysis. In *Proceedings of the IEEE/CVF Winter Conference on Applications of Computer Vision (WACV)*, pages 1970–1980, 2023. [3](#), [7](#), [8](#), [1](#)
- [14] Xiangxiang Chu, Renda Li, and Yong Wang. Usp: Unified self-supervised pretraining for image generation and understanding. In *Proceedings of the IEEE/CVF International Conference on Computer Vision (ICCV)*, pages 18475–18486, 2025. [1](#), [3](#), [5](#)
- [15] Hyungjin Chung, Suhyeon Lee, and Jong Chul Ye. Decomposed diffusion sampler for accelerating large-scale inverse problems. In *The Twelfth International Conference on Learning Representations*, 2024. [3](#)
- [16] Kenneth Clark, Bruce Vendt, Kirk Smith, John Freymann, Justin Kirby, Paul Koppel, Stephen Moore, Stanley Phillips, David Maffitt, Michael Pringle, et al. The cancer imaging archive (tcia): maintaining and operating a public information repository. *Journal of digital imaging*, 26(6):1045–1057, 2013. [5](#), [1](#), [2](#)
- [17] Prafulla Dhariwal and Alexander Nichol. Diffusion models beat gans on image synthesis. In *Advances in Neural Information Processing Systems*, pages 8780–8794, 2021. [1](#)
- [18] Paul Friedrich, Julia Wolleb, Florentin Bieder, Alicia Durrer, and Philippe C Cattin. Wdm: 3d wavelet diffusion models for high-resolution medical image synthesis. In *MICCAI workshop on deep generative models*, pages 11–21. Springer, 2024. [5](#)

- [19] Yaroslav Ganin, Evgeniya Ustinova, Hana Ajakan, Pascal Germain, Hugo Larochelle, François Laviolette, Mario March, and Victor Lempitsky. Domain-adversarial training of neural networks. *Journal of Machine Learning Research*, 17(59):1–35, 2016. 4
- [20] Shanghua Gao, Pan Zhou, Ming-Ming Cheng, and Shuicheng Yan. Masked diffusion transformer is a strong image synthesizer. In *Proceedings of the IEEE/CVF International Conference on Computer Vision (ICCV)*, pages 23164–23173, 2023. 6
- [21] Arthur Gretton, Karsten M. Borgwardt, Malte J. Rasch, Bernhard Schölkopf, and Alexander Smola. A kernel two-sample test. *J. Mach. Learn. Res.*, 13(null):723–773, 2012. 6
- [22] Aaron J Grossberg, Abdallah SR Mohamed, Hesham Elhawalawani, William C Bennett, Kirk E Smith, Tracy S Nolan, Bowman Williams, Sasikarn Chamchod, Jolien Heukelom, Michael E Kantor, et al. Imaging and clinical data archive for head and neck squamous cell carcinoma patients treated with radiotherapy. *Scientific data*, 5(1):1–10, 2018. 5, 1, 2
- [23] Ran Gu, Guotai Wang, Jiangshan Lu, Jingyang Zhang, Wenhui Lei, Yinan Chen, Wenjun Liao, Shichuan Zhang, Kang Li, Dimitris N. Metaxas, and Shaoting Zhang. Cdds: Contrastive domain disentanglement and style augmentation for generalizable medical image segmentation. *Medical Image Analysis*, 89:102904, 2023. 2, 3
- [24] Pengfei Guo, Can Zhao, Dong Yang, Ziyue Xu, Vishwesh Nath, Yucheng Tang, Benjamin Simon, Mason Belue, Stephanie Harmon, Baris Turkbey, and Daguang Xu. Maisi: Medical ai for synthetic imaging. In *2025 IEEE/CVF Winter Conference on Applications of Computer Vision (WACV)*, pages 4430–4441, 2025. 3, 5, 6, 1, 2, 4
- [25] Ibrahim Ethem Hamamci, Sezgin Er, Anjany Sekuboyina, Enis Simsar, Alperen Tezcan, Ayse Gulnihan Simsek, Sevval Nil Esirgun, Furkan Almas, Irem Doğan, Muhammed Furkan Dasdelen, et al. Generatect: Text-conditional generation of 3d chest ct volumes. In *European Conference on Computer Vision*, pages 126–143, 2024. 1
- [26] Ali Hatamizadeh, Vishwesh Nath, Yucheng Tang, Dong Yang, Holger R Roth, and Daguang Xu. Swin unetr: Swin transformers for semantic segmentation of brain tumors in mri images. In *International MICCAI brainlesion workshop*, pages 272–284. Springer, 2021. 7
- [27] Ali Hatamizadeh, Yucheng Tang, Vishwesh Nath, Dong Yang, Andriy Myronenko, Bennett Landman, Holger R. Roth, and Daguang Xu. Unetr: Transformers for 3d medical image segmentation. In *Proceedings of the IEEE/CVF Winter Conference on Applications of Computer Vision (WACV)*, pages 574–584, 2022. 5, 7, 4
- [28] Kaiming He, Haoqi Fan, Yuxin Wu, Saining Xie, and Ross Girshick. Momentum contrast for unsupervised visual representation learning. In *Proceedings of the IEEE/CVF Conference on Computer Vision and Pattern Recognition (CVPR)*, 2020. 1, 7
- [29] Kaiming He, Xinlei Chen, Saining Xie, Yanghao Li, Piotr Dollár, and Ross Girshick. Masked autoencoders are scalable vision learners. In *Proceedings of the IEEE/CVF Conference on Computer Vision and Pattern Recognition (CVPR)*, pages 16000–16009, 2022. 1, 7
- [30] Yuting He, Guanyu Yang, Rongjun Ge, Yang Chen, Jean-Louis Coatrieux, Boyu Wang, and Shuo Li. Geometric visual similarity learning in 3d medical image self-supervised pre-training. In *Proceedings of the IEEE/CVF Conference on Computer Vision and Pattern Recognition (CVPR)*, pages 9538–9547, 2023. 3, 7, 2
- [31] Martin Heusel, Hubert Ramsauer, Thomas Unterthiner, Bernhard Nessler, and Sepp Hochreiter. Gans trained by a two time-scale update rule converge to a local nash equilibrium. In *Advances in Neural Information Processing Systems*, 2017. 6
- [32] Irina Higgins, David Amos, David Pfau, Sebastien Racaniere, Loic Matthey, Danilo Rezende, and Alexander Lerchner. Towards a definition of disentangled representations. *arXiv preprint arXiv:1812.02230*, 2018. 3
- [33] Jonathan Ho and Tim Salimans. Classifier-free diffusion guidance. *arXiv preprint arXiv:2207.12598*, 2022. 6, 2
- [34] Jonathan Ho, Ajay Jain, and Pieter Abbeel. Denoising diffusion probabilistic models. In *Advances in Neural Information Processing Systems*, pages 6840–6851, 2020. 1
- [35] Drew A. Hudson, Daniel Zoran, Mateusz Malinowski, Andrew K. Lampinen, Andrew Jaegle, James L. McClelland, Loic Matthey, Felix Hill, and Alexander Lerchner. Soda: Bottleneck diffusion models for representation learning. In *Proceedings of the IEEE/CVF Conference on Computer Vision and Pattern Recognition (CVPR)*, pages 23115–23127, 2024. 3
- [36] Mahmoud Ibrahim, Yasmina Al Khalil, Sina Amirrajab, Chang Sun, Marcel Breeuwer, Josien Pluim, Bart Elen, Gökhan Ertaylan, and Michel Dumontier. Generative ai for synthetic data across multiple medical modalities: A systematic review of recent developments and challenges. *Computers in Biology and Medicine*, 189:109834, 2025. 2
- [37] Fabian Isensee, Jens Petersen, Andre Klein, David Zimmerer, Paul F Jaeger, Simon Kohl, Jakob Wasserthal, Gregor Koehler, Tobias Norajitra, Sebastian Wirkert, et al. nnu-net: Self-adapting framework for u-net-based medical image segmentation. *arXiv preprint arXiv:1809.10486*, 2018. 6, 7
- [38] Yuanfeng Ji, Haotian Bai, Chongjian GE, Jie Yang, Ye Zhu, Ruimao Zhang, Zhen Li, Lingyan Zhanng, Wanling Ma, Xi-ang Wan, and Ping Luo. Amos: A large-scale abdominal multi-organ benchmark for versatile medical image segmentation. In *Advances in Neural Information Processing Systems*, pages 36722–36732, 2022. 5, 2
- [39] Yankai Jiang, Mingze Sun, Heng Guo, Xiaoyu Bai, Ke Yan, Le Lu, and Minfeng Xu. Anatomical invariance modeling and semantic alignment for self-supervised learning in 3d medical image analysis. In *Proceedings of the IEEE/CVF International Conference on Computer Vision (ICCV)*, pages 15859–15869, 2023. 3
- [40] Prannay Khosla, Piotr Teterwak, Chen Wang, Aaron Sarna, Yonglong Tian, Phillip Isola, Aaron Maschinot, Ce Liu, and Dilip Krishnan. Supervised contrastive learning. In *Advances in Neural Information Processing Systems*, pages 18661–18673, 2020. 5

- [41] Hyunjik Kim and Andriy Mnih. Disentangling by factorising. In *Proceedings of the 35th International Conference on Machine Learning*, pages 2649–2658. PMLR, 2018. 3
- [42] Bennett Landman, Zhoubing Xu, Juan Igelsias, Martin Styner, Thomas Langerak, and Arno Klein. Miccai multi-atlas labeling beyond the cranial vault—workshop and challenge. In *Proc. MICCAI multi-atlas labeling beyond cranial vault—workshop challenge*, page 12. Munich, Germany, 2015. 5, 1, 2
- [43] Jihao Liu, Xin Huang, Jinliang Zheng, Yu Liu, and Hongsheng Li. Mixmae: Mixed and masked autoencoder for efficient pretraining of hierarchical vision transformers. In *Proceedings of the IEEE/CVF Conference on Computer Vision and Pattern Recognition (CVPR)*, pages 6252–6261, 2023. 4
- [44] Xiao Liu, Pedro Sanchez, Spyridon Thermos, Alison Q. O’Neil, and Sotirios A. Tsaftaris. Learning disentangled representations in the imaging domain. *Medical Image Analysis*, 80:102516, 2022. 2
- [45] Francesco Locatello, Stefan Bauer, Mario Lucic, Gunnar Raetsch, Sylvain Gelly, Bernhard Schölkopf, and Olivier Bachem. Challenging common assumptions in the unsupervised learning of disentangled representations. In *Proceedings of the 36th International Conference on Machine Learning*, pages 4114–4124. PMLR, 2019. 3
- [46] Ilya Loshchilov and Frank Hutter. Decoupled weight decay regularization. In *International Conference on Learning Representations*, 2019. 5
- [47] Xiangde Luo, Wenjun Liao, Jianghong Xiao, Jieneng Chen, Tao Song, Xiaofan Zhang, Kang Li, Dimitris N. Metaxas, Guotai Wang, and Shaoting Zhang. Word: A large scale dataset, benchmark and clinical applicable study for abdominal organ segmentation from ct image. *Medical Image Analysis*, 82:102642, 2022. 5, 2
- [48] Jun Ma, Yao Zhang, Song Gu, Cheng Ge, Ershuai Wang, Qin Zhou, Ziyang Huang, Pengju Lyu, Jian He, and Bo Wang. Automatic organ and pan-cancer segmentation in abdomen ct: the flare 2023 challenge. *arXiv preprint arXiv:2408.12534*, 2024. 5, 1, 2
- [49] Nanye Ma, Mark Goldstein, Michael S Albergo, Nicholas M Boffi, Eric Vanden-Eijnden, and Saining Xie. Sit: Exploring flow and diffusion-based generative models with scalable interpolant transformers. In *European Conference on Computer Vision*, pages 23–40. Springer, 2024. 5, 2
- [50] Ye Mao, Lan Jiang, Xi Chen, and Chao Li. Disc-diff: Disentangled conditional diffusion model for multi-contrast mri super-resolution. In *International Conference on Medical Image Computing and Computer-Assisted Intervention*, pages 387–397. Springer, 2023. 3
- [51] Soumik Mukhopadhyay, Matthew Gwilliam, Yosuke Yamaguchi, Vatsal Agarwal, Namitha Padmanabhan, Archana Swaminathan, Tianyi Zhou, Jun Ohya, and Abhinav Shrivastava. Do text-free diffusion models learn discriminative visual representations? In *European Conference on Computer Vision*, pages 253–272, 2024. 3
- [52] Sarah Müller, Lisa M. Koch, Hendrik P.A. Lensch, and Philipp Berens. Disentangling representations of retinal images with generative models. *Medical Image Analysis*, 105:103628, 2025. 2, 3
- [53] Maxime Oquab, Timothée Darcet, Théo Moutakanni, Huy V. Vo, Marc Szafraniec, Vasil Khalidov, Pierre Fernandez, Daniel HAZIZA, Francisco Massa, Alaeldin El-Nouby, Mido Assran, Nicolas Ballas, Wojciech Galuba, Russell Howes, Po-Yao Huang, Shang-Wen Li, Ishan Misra, Michael Rabbat, Vasu Sharma, Gabriel Synnaeve, Hu Xu, Herve Jegou, Julien Mairal, Patrick Labatut, Armand Joulin, and Piotr Bojanowski. DINOv2: Learning robust visual features without supervision. *Transactions on Machine Learning Research*, 2024. Featured Certification. 1
- [54] Mathias Öttl, Frauke Wilm, Jana Steenpass, Jingna Qiu, Matthias Rübner, Arndt Hartmann, Matthias Beckmann, Peter Fasching, Andreas Maier, Ramona Erber, et al. Style-extracting diffusion models for semi-supervised histopathology segmentation. In *European Conference on Computer Vision*, pages 236–252, 2024. 2
- [55] William Peebles and Saining Xie. Scalable diffusion models with transformers. In *Proceedings of the IEEE/CVF International Conference on Computer Vision (ICCV)*, pages 4195–4205, 2023. 5, 2, 3
- [56] Kunpeng Qiu, Zhiqiang Gao, Zhiying Zhou, Mingjie Sun, and Yongxin Guo. Noise-consistent siamese-diffusion for medical image synthesis and segmentation. In *Proceedings of the IEEE/CVF Conference on Computer Vision and Pattern Recognition (CVPR)*, pages 15672–15681, 2025. 3
- [57] Zelin Qiu, Xi Wang, Zhuoyao Xie, Juan Zhou, Yu Wang, Lingjie Yang, Xinrui Jiang, Juyoung Bae, Moo Hyun Son, Qiang Ye, et al. Large-scale multi-sequence pretraining for generalizable mri analysis in versatile clinical applications. *arXiv preprint arXiv:2508.07165*, 2025. 3
- [58] Rahul Ravishankar, Zeeshan Patel, Jathushan Rajasegaran, and Jitendra Malik. Scaling properties of diffusion models for perceptual tasks. In *Proceedings of the IEEE/CVF Conference on Computer Vision and Pattern Recognition (CVPR)*, pages 12945–12954, 2025. 3
- [59] Marie-Pierre Revel, Samia Boussouar, Constance de Margerie-Mellon, Inès Saab, Thibaut Lapotre, Dominique Mompont, Guillaume Chassagnon, Audrey Milon, Mathieu Lederlin, Souhail Bennani, et al. Study of thoracic ct in covid-19: The stoic project. *Radiology*, 301(1):E361–E370, 2021. 5, 1, 2
- [60] Robin Rombach, Andreas Blattmann, Dominik Lorenz, Patrick Esser, and Björn Ommer. High-resolution image synthesis with latent diffusion models. In *Proceedings of the IEEE/CVF Conference on Computer Vision and Pattern Recognition (CVPR)*, pages 10684–10695, 2022. 1
- [61] Shaohao Rui, Lingzhi Chen, Zhenyu Tang, Lilong Wang, Mianxin Liu, Shaoting Zhang, and Xiaosong Wang. Multimodal vision pre-training for medical image analysis. In *Proceedings of the IEEE/CVF Conference on Computer Vision and Pattern Recognition (CVPR)*, pages 5164–5174, 2025. 3
- [62] Arnaud Arindra Adiyoso Setio, Alberto Traverso, Thomas de Bel, Moira S.N. Berens, Cas van den Bogaard, Piergiorgio Cerello, Hao Chen, Qi Dou, Maria Evelina Fantacci, Bram Geurts, Robbert van der Gugten, Pheng Ann Heng, Bart Jansen, Michael M.J. de Kaste, Valentin Kotov, Jack Yu-Hung Lin, Jeroen T.M.C. Manders, Alexander Sónora-Mengana, Juan Carlos García-Naranjo, Evge-

- nia Papavasileiou, Mathias Prokop, Marco Saletta, Cornelia M Schaefer-Prokop, Ernst T. Scholten, Luuk Scholten, Miranda M. Snoeren, Ernesto Lopez Torres, Jef Vande-meulebroucke, Nicole Walasek, Guido C.A. Zuidhof, Bram van Ginneken, and Colin Jacobs. Validation, comparison, and combination of algorithms for automatic detection of pulmonary nodules in computed tomography images: The luna16 challenge. *Medical Image Analysis*, 42:1–13, 2017. 5, 1, 2
- [63] Amber L Simpson, Michela Antonelli, Spyridon Bakas, Michel Bilello, Keyvan Farahani, Bram Van Ginneken, Annette Kopp-Schneider, Bennett A Landman, Geert Litjens, Bjoern Menze, et al. A large annotated medical image dataset for the development and evaluation of segmentation algorithms. *arXiv preprint arXiv:1902.09063*, 2019. 5, 1, 2
- [64] Zhenxiong Tan, Songhua Liu, Xingyi Yang, Qiaochu Xue, and Xinchao Wang. Ominicontrol: Minimal and universal control for diffusion transformer. In *Proceedings of the IEEE/CVF International Conference on Computer Vision (ICCV)*, pages 14940–14950, 2025. 6
- [65] Fenghe Tang, Qingsong Yao, Wenxin Ma, Chenxu Wu, Zihang Jiang, and S. Kevin Zhou. Hi-end-mae: Hierarchical encoder-driven masked autoencoders are stronger vision learners for medical image segmentation. *Medical Image Analysis*, 107:103770, 2026. 2, 3, 5, 7, 8, 1, 4
- [66] Youbao Tang, Yuxing Tang, Yingying Zhu, Jing Xiao, and Ronald M. Summers. A disentangled generative model for disease decomposition in chest x-rays via normal image synthesis. *Medical Image Analysis*, 67:101839, 2021. 3
- [67] Piyush Tiwary, Kinjawl Bhattacharyya, and Prathosh AP. LangDAug: Langevin data augmentation for multi-source domain generalization in medical image segmentation. In *Forty-second International Conference on Machine Learning*, 2025. 2
- [68] Tassilo Wald, Constantin Ulrich, Stanislav Lukyanenko, Andrei Goncharov, Alberto Paderno, Maximilian Miller, Leander Maerkisch, Paul Jaeger, and Klaus Maier-Hein. Revisiting mae pre-training for 3d medical image segmentation. In *Proceedings of the IEEE/CVF Conference on Computer Vision and Pattern Recognition (CVPR)*, pages 5186–5196, 2025. 2
- [69] Haoshen Wang, Zhentao Liu, Kaicong Sun, Xiaodong Wang, Dinggang Shen, and Zhiming Cui. 3d meddiffusion: A 3d medical latent diffusion model for controllable and high-quality medical image generation. *IEEE Transactions on Medical Imaging*, pages 1–1, 2025. 1, 3, 5, 6, 4
- [70] Jindong Wang, Cuiling Lan, Chang Liu, Yidong Ouyang, Tao Qin, Wang Lu, Yiqiang Chen, Wenjun Zeng, and Philip S. Yu. Generalizing to unseen domains: A survey on domain generalization. *IEEE Transactions on Knowledge and Data Engineering*, 35(8):8052–8072, 2023. 2
- [71] Jinglong Wang, Xiawei Li, Jing Zhang, Qingyuan Xu, Qin Zhou, Qian Yu, Lu Sheng, and Dong Xu. Diffusion model is secretly a training-free open vocabulary semantic segmenter. *IEEE Transactions on Image Processing*, 34:1895–1907, 2025. 3
- [72] Siwen Wang, Churan Wang, Fei Gao, Lixian Su, Fandong Zhang, Yizhou Wang, and Yizhou Yu. Autoregressive sequence modeling for 3d medical image representation. *Proceedings of the AAAI Conference on Artificial Intelligence*, 39(8):7871–7879, 2025. 3
- [73] Xin Wang, Hong Chen, Si’ao Tang, Zihao Wu, and Wenwu Zhu. Disentangled representation learning. *IEEE Transactions on Pattern Analysis and Machine Intelligence*, 46(12):9677–9696, 2024. 3
- [74] Yiqing Wang, Zihan Li, Jieru Mei, Zihao Wei, Li Liu, Chen Wang, Shengtian Sang, Alan L Yuille, Cihang Xie, and Yuyin Zhou. Swinmm: masked multi-view with swin transformers for 3d medical image segmentation. In *International conference on medical image computing and computer-assisted intervention*, pages 486–496. Springer, 2023. 7
- [75] Yuran Wang, Zhijing Wan, Yansheng Qiu, and Zheng Wang. Devil is in details: Locality-aware 3d abdominal ct volume generation for self-supervised organ segmentation. In *Proceedings of the 32nd ACM International Conference on Multimedia*, page 10640–10648, 2024. 2
- [76] Z. Wang, E.P. Simoncelli, and A.C. Bovik. Multiscale structural similarity for image quality assessment. In *The Thirty-Seventh Asilomar Conference on Signals, Systems & Computers, 2003*, pages 1398–1402 Vol.2, 2003. 6
- [77] Jakob Wasserthal, Hanns-Christian Breit, Manfred T Meyer, Maurice Pradella, Daniel Hinck, Alexander W Sauter, Tobias Heye, Daniel T Boll, Joshy Cyriac, Shan Yang, et al. Totalsegmentator: robust segmentation of 104 anatomic structures in ct images. *Radiology: Artificial Intelligence*, 5(5):e230024, 2023. 5, 6, 1, 2
- [78] Chen Wei, Kartikeya Mangalam, Po-Yao Huang, Yanghao Li, Haoqi Fan, Hu Xu, Huiyu Wang, Cihang Xie, Alan Yuille, and Christoph Feichtenhofer. Diffusion models as masked autoencoders. In *Proceedings of the IEEE/CVF International Conference on Computer Vision (ICCV)*, pages 16284–16294, 2023. 1, 3
- [79] Linshan Wu, Jiaxin Zhuang, and Hao Chen. Voco: A simple-yet-effective volume contrastive learning framework for 3d medical image analysis. In *Proceedings of the IEEE/CVF Conference on Computer Vision and Pattern Recognition (CVPR)*, pages 22873–22882, 2024. 1, 2, 3, 5, 7, 4
- [80] Linshan Wu, Jiaxin Zhuang, and Hao Chen. Large-scale 3d medical image pre-training with geometric context priors. *arXiv preprint arXiv:2410.09890*, 2024. 2, 5
- [81] Mengqi Wu, Lintao Zhang, Pew-Thian Yap, Hongtu Zhu, and Mingxia Liu. Disentangled latent energy-based style translation: An image-level structural mri harmonization framework. *Neural Networks*, 184:107039, 2025. 3
- [82] Weilai Xiang, Hongyu Yang, Di Huang, and Yunhong Wang. Denoising diffusion autoencoders are unified self-supervised learners. In *Proceedings of the IEEE/CVF International Conference on Computer Vision (ICCV)*, pages 15802–15812, 2023. 1, 3
- [83] Zhenda Xie, Zheng Zhang, Yue Cao, Yutong Lin, Jianmin Bao, Zhuliang Yao, Qi Dai, and Han Hu. Simmim: A simple framework for masked image modeling. In *Proceedings of the IEEE/CVF Conference on Computer Vision and Pattern Recognition (CVPR)*, pages 9653–9663, 2022. 7

- [84] Yanwu Xu, Li Sun, Wei Peng, Shuyue Jia, Katelyn Morrison, Adam Perer, Afrooz Zandifar, Shyam Visweswaran, Motahare Eslami, and Kayhan Batmanghelich. Medsyn: Text-guided anatomy-aware synthesis of high-fidelity 3-d ct images. *IEEE Transactions on Medical Imaging*, 43(10):3648–3660, 2024. 5
- [85] Siyuan Yan, Zhen Yu, Chi Liu, Lie Ju, Dwarikanath Mahapatra, Brigid Betz-Stablein, Victoria Mar, Monika Janda, Peter Soyer, and Zongyuan Ge. Prompt-driven latent domain generalization for medical image classification. *IEEE Transactions on Medical Imaging*, 44(1):348–360, 2025. 2, 3
- [86] Tao Yang, Cuiling Lan, Yan Lu, and Nanning Zheng. Diffusion model with cross attention as an inductive bias for disentanglement. In *Advances in Neural Information Processing Systems*, pages 82465–82492, 2024. 3
- [87] Jingfeng Yao, Bin Yang, and Xinggong Wang. Reconstruction vs. generation: Taming optimization dilemma in latent diffusion models. In *Proceedings of the IEEE/CVF Conference on Computer Vision and Pattern Recognition (CVPR)*, pages 15703–15712, 2025. 6
- [88] Yousef Yeganeh, Azade Farshad, Ioannis Charisiadis, Marta Hasny, Martin Hartenberger, Björn Ommer, Nassir Navab, and Ehsan Adeli. Latent drifting in diffusion models for counterfactual medical image synthesis. In *Proceedings of the IEEE/CVF Conference on Computer Vision and Pattern Recognition (CVPR)*, pages 7685–7695, 2025. 3
- [89] Sihyun Yu, Sangkyung Kwak, Huiwon Jang, Jongheon Jeong, Jonathan Huang, Jinwoo Shin, and Saining Xie. Representation alignment for generation: Training diffusion transformers is easier than you think. In *The Thirteenth International Conference on Learning Representations*, 2025. 6
- [90] An Zhang, Han Wang, Xiang Wang, and Tat-Seng Chua. Disentangling masked autoencoders for unsupervised domain generalization. In *European Conference on Computer Vision*, pages 126–151, 2024. 2
- [91] Kang Zhang, Xiaohong Liu, Jun Shen, Zhihuan Li, Ye Sang, Xingwang Wu, Yunfei Zha, Wenhua Liang, Chengdi Wang, Ke Wang, et al. Clinically applicable ai system for accurate diagnosis, quantitative measurements, and prognosis of covid-19 pneumonia using computed tomography. *Cell*, 181(6):1423–1433, 2020. 5, 2
- [92] Lvmin Zhang, Anyi Rao, and Maneesh Agrawala. Adding conditional control to text-to-image diffusion models. In *Proceedings of the IEEE/CVF International Conference on Computer Vision (ICCV)*, pages 3836–3847, 2023. 6
- [93] Qilong Zhao, Yifei Zhang, Mengdan Zhu, Siyi Gu, Yuyang Gao, Xiaofeng Yang, and Liang Zhao. Due: Dynamic uncertainty-aware explanation supervision via 3d imputation. In *Proceedings of the 30th ACM SIGKDD Conference on Knowledge Discovery and Data Mining*, page 6335–6343, 2024. 2
- [94] Hongkai Zheng, Weili Nie, Arash Vahdat, and Anima Anandkumar. Fast training of diffusion models with masked transformers. *Transactions on Machine Learning Research*, 2024. 6
- [95] Jiaxin Zhuang, Luyang Luo, Qiong Wang, Mingxiang Wu, Lin Luo, and Hao Chen. Advancing volumetric medical image segmentation via global-local masked autoencoders. *IEEE Transactions on Medical Imaging*, pages 1–1, 2025. 5, 7, 8, 1, 2, 3
- [96] Jiaxin Zhuang, Linshan Wu, Qiong Wang, Peng Fei, Varut Vardhanabhuti, Lin Luo, and Hao Chen. Mim: Mask in mask self-supervised pre-training for 3d medical image analysis. *IEEE Transactions on Medical Imaging*, 44(9):3727–3740, 2025. 3, 5, 7, 1, 2, 4
- [97] Xiahai Zhuang. Multivariate mixture model for myocardial segmentation combining multi-source images. *IEEE Transactions on Pattern Analysis and Machine Intelligence*, 41(12):2933–2946, 2019. 5, 1, 2

MeDUET: Disentangled Unified Pretraining for 3D Medical Image Synthesis and Analysis

Supplementary Material

This supplementary material is organized as follows:

- Section A presents the full pretraining algorithm of MeDUET.
- Section B describes the pretraining datasets and downstream analysis datasets.
- Section C provides additional training and implementation details, including factor extraction for downstream tasks, dual classifier-free guidance for synthesis, and the style augmentation scheme for analysis.
- Section D reports a computational analysis comparing FLOPs, wall-clock time, and overall efficiency with existing medical SSL baselines.
- Section E presents additional experiments, including ablations on the VAE tokenizer, factor effectiveness and generalization, and failure case analysis.
- Section F provides discussions on domain configurations, empirical factor identifiability, and remaining limitations.

A. Algorithm

Algorithm 1 illustrates the detailed pretraining procedure of MeDUET.

B. Datasets

B.1. Pretraining Datasets

Details of the pretraining VoCo-10k dataset are provided in Table 7. Specifically, VoCo-10k comprises 10 public datasets: BTCV [42], MM-WHS [97], Spleen [63], TCIA Covid19 [16], LUNA16 [62], STOIC 2021 [59], FLARE23 [48], LiDC [1], HNSCC [22], and TotalSegmentator [77]. We follow the previously released open-source data splits [79, 95, 96] for the pretraining datasets to ensure consistency and fair comparison.

B.2. Downstream Analysis Task Datasets

For downstream analysis tasks, we perform a comprehensive evaluation on four datasets covering both segmentation and classification across two modalities. Details of the downstream datasets used in the analysis tasks are provided in Table 8. We also follow the data splits used in prior work [65, 79] to ensure fair comparison.

C. Additional Training Details

C.1. Implementation Details

All experiments are implemented using PyTorch and MONAI, and training is conducted on four NVIDIA A100

Algorithm 1 Pretraining procedure of MeDUET

Require: Dataset with multi domains and domain labels; VAE encoder; MeDUET student model; EMA teacher model.

Ensure: Model parameters of student network.

- Initialize model parameters.
- 1: **for** each training iteration **do**
 - 2: Sample two batches $\{\mathbf{x}_i, \mathbf{x}_j\}$ and encode into latent tokens $\{\mathbf{z}_i, \mathbf{z}_j\}$ by the VAE.
▷ Demixing & Dual Reconstruction
 - 3: Mix and encode tokens $\mathbf{z}_{ij}^{mix} = \phi_m(\mathbf{z}_i, \mathbf{z}_j, M)$, $\mathbf{z}_i^e, \mathbf{z}_j^e = \phi_u(\mathcal{F}_{enc}(\mathbf{z}_{ij}^{mix}), M)$.
 - 4: Apply \mathcal{F}_d and \mathcal{F}_{dec} to obtain factors $(\mathbf{c}_i, \mathbf{s}_i, \mathbf{c}_j, \mathbf{s}_j)$, and reconstructed tokens $(\hat{\mathbf{z}}_i, \hat{\mathbf{z}}_j)$.
 - 5: Compute the dual reconstruction loss \mathcal{L}_r by Eq. (1).
▷ Factor Disentanglement
 - 6: Obtain disentangled factors by convolution $(\mathbf{c}_i, \mathbf{s}_i), (\mathbf{c}_j, \mathbf{s}_j) = \text{conv}(\mathbf{z}_i^e), \text{conv}(\mathbf{z}_j^e)$.
 - 7: Compute domain classifier loss \mathcal{L}_d by Eq. (2).
 - 8: Re-aggregate factors to tokens $\hat{\mathbf{z}}_i^e = \text{conv}(\mathbf{c}_i, \mathbf{s}_i)$, $\hat{\mathbf{z}}_j^e = \text{conv}(\mathbf{c}_j, \mathbf{s}_j)$.
▷ MFTD
 - 9: Re-encode $(\hat{\mathbf{z}}_i, \hat{\mathbf{z}}_j)$ with student and teacher branches (teacher stop-gradient) to obtain student factors $(\hat{\mathbf{c}}_i, \hat{\mathbf{s}}_i, \hat{\mathbf{c}}_j, \hat{\mathbf{s}}_j)$ and teacher factors $(\hat{\mathbf{c}}_i^T, \hat{\mathbf{s}}_i^T, \hat{\mathbf{c}}_j^T, \hat{\mathbf{s}}_j^T)$.
 - 10: Distill tokens of mixed regions using $\mathcal{L}_{\text{MFTD}}$ by Eq. (6).
▷ SiQC
 - 11: Generate swapped tokens $\mathbf{z}_{ij} = \mathcal{F}_{dec}(\text{conv}(\mathbf{c}_i, \mathbf{s}_j))$, $\mathbf{z}_{ji} = \mathcal{F}_{dec}(\text{conv}(\mathbf{c}_j, \mathbf{s}_i))$.
 - 12: Re-encode $\{\mathbf{z}_i, \mathbf{z}_j, \mathbf{z}_{ij}, \mathbf{z}_{ji}\}$ to obtain pooled content/style factors $\{\mathbf{q}_c, \mathbf{k}_c, \mathbf{q}_s, \mathbf{k}_s\}$ and construct the quadruplet $\mathcal{V}(i, j)$.
 - 13: Build positive masks in content/style spaces and compute $\mathcal{L}_{\text{SiQC}}$ by Eq. (12).
 - 14: Compute total loss \mathcal{L} by Eq. (13).
 - 15: Update the student model with \mathcal{L} and update the teacher model by EMA.
 - 16: **end for**
-

GPUs. Following previous works [13, 65, 95], we adopt ViT-B as the backbone encoder of MeDUET, which is an appropriate choice given the dataset scale. The input and output channels are modified to 4 to match the latent dimensionality of our VAE tokenizer [24]. The class tokens are discarded in all downstream applications. The remain-

Table 7. The details of pretraining datasets.

Dataset	Modality	Region of Interest	#Volumes
BTCV [42]	CT	Abdomen	24
MM-WHS [97]	CT	Chest	16
Spleen [63]	CT	Spleen	32
TCIA Covid19 [16]	CT	Chest	722
LUNA16 [62]	CT	Chest	843
STOIC 2021 [59]	CT	Chest	2000
FLARE23 [48]	CT	Abdomen	4000
LiDC [1]	CT	Chest	589
HNSCC [22]	CT	Head/Neck	1071
TotalSegmentator [77]	CT	Head/Neck/Chest/leg/ Abdomen/pelvis/feet	1203

Table 8. The details of downstream analysis datasets.

Dataset	Modality	#Train					#Valid
		Full	1-shot	10%	50%	100%	
AMOS [38]	CT	240	1	24	120	240	120
WORD [47]	CT	100	1	10	50	100	20
BraTS21 [3]	MRI	1000	1	100	500	1000	251
CC-CII [91]	CT	2514	1	251	1257	2514	1664

ing experimental settings follow prior methods [30, 65, 79, 95, 96] for fair comparison.

The dimensions of the content and style representations, D_c , D_s , are set to 768 and 192, respectively. The hyperparameters of the loss functions are set as follows: $\lambda_1 = 0.2$, $\lambda_2 = 0.5$, $\lambda_3 = 0.3$, and $\lambda_c = 0.5$. The GRL strength of the domain classifier is set to 1.0. For the EMA teacher, the decay rate is initialized at 0.997 and gradually increased to 0.9997 during pretraining using a cosine schedule. Details of the pre-processing and pretraining settings are provided in Table 9.

C.2. Factor Generation for Downstream Applications

We extract the content and style vectors for each volume for use in downstream tasks. Specifically, each volume is cropped into fixed-size sub-volumes and fed into the frozen MeDUET model, where the factor disentanglement module produces content and style representations $\mathbf{c} \in \mathbb{R}^{L \times D_c}$ and $\mathbf{s} \in \mathbb{R}^{L \times D_s}$. The sub-volume size is kept identical to the pre-processing configuration (i.e., $96 \times 96 \times 96$) to ensure consistency. The resulting content and style representations from all sub-volumes are then aggregated at the volume level. With the sub-volumes covering the full volume, we apply patch-level and token-level mean pooling to the aggregated representations, yielding the final content and style vectors $\mathbf{c}_0 \in \mathbb{R}^{D_c}$ and $\mathbf{s}_0 \in \mathbb{R}^{D_s}$, which capture the domain-invariant anatomical information and domain-discriminative style characteristics of the entire volume, respectively.

Table 9. The overview of pre-processing and pretraining settings in the experiments.

Pre-processing Settings	
Spacing	$1.5 \times 1.5 \times 1.5$
Intensity	$[-175, 250]$
Norm	$[0, 1]$
Sub-volume size	$96 \times 96 \times 96$
Latent size	$4 \times 24 \times 24 \times 24$
Augmentation	Random Rotate and Flip
Pretraining Settings	
Pretraining steps	200k
Optimizer	AdamW
Weight decay	$1e-2$
Optimizer momentum	$\beta_1, \beta_2 = 0.9, 0.95$
Optimizer lr	$1e-4$
Batch size	$64 \times 4 = 256$
Lr schedule	Warmup cosine
Warmup steps	2k
Factor dimension	$D_c, D_s = 768, 192$
Loss coefficients	$\lambda_1, \lambda_2, \lambda_3, \lambda_c = 0.2, 0.5, 0.3, 0.5$
EMA decay	0.997, 0.9997
GRL coefficient	1.0

C.3. Downstream Synthesis

Hyperparameters. For the diffusion-based synthesis task, we build our model upon the original DiT and SiT implementations and adopt the same hyperparameter configurations [49, 55]. The latent representations and factor codes are precomputed using MAISI-VAE [24] and MeDUET, respectively. The hyperparameter settings of DiT/SiT used in our generation experiments are summarized in Table 10. During both training and sampling, we apply dual classifier-free dropout and dual CFG conditioning [33] based on the learned disentangled content and style codes.

Training: Dual Classifier-Free Dropout. Given a 3D volume, our frozen MeDUET produces a content vector $\mathbf{c}_0 \in \mathbb{R}^{D_c}$ and a style vector $\mathbf{s}_0 \in \mathbb{R}^{D_s}$. We standardize each vector with per-sample L_2 normalization and temperature scaling as

$$\text{norm}_\tau(v) = \frac{v}{\|v\|_2 + \varepsilon} \cdot \frac{1}{\tau}, \quad (14)$$

$$\hat{\mathbf{c}} = \text{norm}_{\tau_c}(\mathbf{c}_0), \quad \hat{\mathbf{s}} = \text{norm}_{\tau_s}(\mathbf{s}_0), \quad (15)$$

where $\tau_c, \tau_s > 0$ are learnable scalars. We maintain learnable null embeddings $\mathbf{c}_\emptyset \in \mathbb{R}^{D_c}$, $\mathbf{s}_\emptyset \in \mathbb{R}^{D_s}$, which pass through the same normalization path: $\hat{\mathbf{c}}_\emptyset = \text{norm}_{\tau_c}(\mathbf{c}_\emptyset)$, $\hat{\mathbf{s}}_\emptyset = \text{norm}_{\tau_s}(\mathbf{s}_\emptyset)$. At each step we draw independent Bernoulli masks for content and style:

$$m_c \sim \text{Bernoulli}(1-p_c), \quad m_s \sim \text{Bernoulli}(1-p_s), \quad (16)$$

with drop probabilities $p_c, p_s \in [0, 1]$, which are set to 0.2 in our model. The conditional vectors used by the diffusion

Table 10. The overview of downstream synthesis settings in the experiments.

	DiT-B/4	SiT-B/4
Pre-processing		
Spacing	$1.5 \times 1.5 \times 1.5$	$1.5 \times 1.5 \times 1.5$
Intensity	$[-175, 250]$	$[-175, 250]$
Norm	$[0, 1]$	$[0, 1]$
Sub-volume size	$256 \times 256 \times 128$	$256 \times 256 \times 128$
Latent size	$4 \times 64 \times 64 \times 32$	$4 \times 64 \times 64 \times 32$
Architecture		
Input dim.	$4 \times 64 \times 64 \times 32$	$4 \times 64 \times 64 \times 32$
Hidden dim.	768	768
Num. blocks	12	12
Num. heads	12	12
Patch size	4	4
Optimization		
Batch size	$16 \times 4 = 64$	$16 \times 4 = 64$
Optimizer	AdamW	AdamW
Lr	$5e-5$	$5e-5$
(β_1, β_2)	(0.9, 0.999)	(0.9, 0.999)
Lr schedule	Warmup cosine	Warmup cosine
Training steps	2M	2M
EMA decay	0.9999	0.9999
Interpolants		
α_t	$1 - t$	-
σ_t	t	-
ω_t	σ_t	-
T	-	1000
Training objective	v-prediction	noise-prediction
Sampler	Euler-Maruyama	DDPM
Sampling steps	250	250
Dropout prob	$p_c, p_s = 0.2, 0.2$	$p_c, p_s = 0.2, 0.2$
Guidance	$w_c, w_s = 3.0, 3.0$	$w_c, w_s = 3.0, 3.0$

transformer (DiT/SiT) are

$$\tilde{c} = m_c \hat{c} + (1 - m_c) \hat{c}_\emptyset, \quad \tilde{s} = m_s \hat{s} + (1 - m_s) \hat{s}_\emptyset. \quad (17)$$

We inject (\tilde{c}, \tilde{s}) via dual-branch AdaLN-Zero [55]. For each block we predict affine/gate parameters from content/style and combine them:

$$(\gamma^c, \beta^c) = W_c \tilde{c}, \quad (\gamma^s, \beta^s) = W_s \tilde{s}, \quad (18)$$

$$\gamma = \gamma^c + \gamma^s, \quad \beta = \beta^c + \beta^s, \quad (19)$$

Given pre-LN activations h , AdaLN-Zero modulation is

$$\text{AdaLN}(h) = (1 + \gamma) \odot \text{LN}(h) + \beta. \quad (20)$$

Sampling: Dual CFG. For a target pair (c_i, s_j) (e.g., content and style from reference cases), we form normalized \hat{c}_i, \hat{s}_j and their null counterparts $\hat{c}_\emptyset, \hat{s}_\emptyset$. At each time step we compute three model evaluations:

$$e_{cs} = \epsilon_\theta(\mathbf{z}_t, t; \hat{c}_i, \hat{s}_j), \quad (21)$$

$$e_{ns} = \epsilon_\theta(\mathbf{z}_t, t; \hat{c}_\emptyset, \hat{s}_j), \quad (22)$$

$$e_{cn} = \epsilon_\theta(\mathbf{z}_t, t; \hat{c}_i, \hat{s}_\emptyset), \quad (23)$$

Table 11. The overview of downstream analysis settings in the experiments.

Pre-processing Settings	
Spacing	$1.5 \times 1.5 \times 1.5$
Intensity	$[-175, 250]$
Norm	$[0, 1]$
Sub-volume size	$96 \times 96 \times 96$
Latent size	$4 \times 24 \times 24 \times 24$
Num. sub-crops	4
Augmentation	Random Rotate, Flip, Scale, Shift
Fine-tuning Settings	
Optimizer	AdamW
Weight decay	$1e-5$
Optimizer momentum	$\beta_1, \beta_2 = 0.9, 0.999$
Optimizer lr	$2e-4$
Batch size	$1 \times 4 = 4$
Inference	Sliding Window Inference
Inference overlap	0.5
Sw batch size	32

Table 12. The hyperparameter settings of style augmentation under different data ratios in the downstream analysis tasks.

Config	Data Ratios			
	1-shot	10%	50%	100%
p_{aug}	0.9	0.8	0.6	0.3
$\alpha_{\text{min}}, \alpha_{\text{max}}$	0.4, 0.8	0.4, 0.8	0.3, 0.6	0.2, 0.5
λ_{aug}	0.4	0.4	0.4	0.4
λ_{cons}	0.3	0.3	0.3	0.3
EMA decay	0.90	0.90	0.90	0.90

where \mathbf{z}_t denotes the input of diffusion transformers, and t is the timestep. We then apply dual guidance with independent strengths $w_c, w_s \geq 0$:

$$\epsilon_{\text{CFG}} = e_{cs} + w_c(e_{cs} - e_{ns}) + w_s(e_{cs} - e_{cn}). \quad (24)$$

Setting $w_c = w_s = 0$ yields near unconditional sampling. In our experiment, we set $w_c = 3.0$ and $w_s = 3.0$ by default. To sum up, our dual CFG design lets us (i) train with missing-condition robustness through the dual CF-dropout, and (ii) perform finely controllable generation at inference time with independent knobs for content consistency and style strength, all while keeping the content/style semantics disentangled.

C.4. Downstream Analysis

Hyperparameters. Following prior work [65, 79, 95, 96], the fine-tuning setups for the analysis tasks are kept largely consistent with the pretraining configurations, as summarized in Table 11. For segmentation tasks, the latent-space outputs of UNETR are passed through the VAE decoder to

Table 13. The computational cost and wall-clock time comparison of medical SSL methods.

Method	Backbone	Param. (M)	Flops (G)	Per Epoch Time (s)	Pretrain Time (GPU hours)	Dice Score (%) \uparrow				Accuracy (%) \uparrow
						BTCV	AMOS	WORD	BraTS21	CC-CCH
VoCo [79]	Swin-B	127.44	1264.9	1867.3	331.9	85.31	85.51	87.53	77.72	90.72
MIM [96]	ViT-B	71.0	1002.5	615.4	683.8	84.07	84.90	87.68	76.77	88.35
Hi-End-MAE [65]	ViT-B	98.9	133.9	164.6	731.6	84.86	85.80	89.37	76.93	86.50
MeDUET	ViT-B	105.1	50.1	72.9	405.2	88.02	86.34	90.07	78.02	91.35

reconstruct the predicted segmentation masks. For classification tasks, we remove the VAE decoder and modify the final output layer of UNETR [27] to directly produce the predictive logits. Moreover, we further evaluate our disentangled latent space on downstream analysis by introducing a style augmentation scheme for both segmentation and classification tasks.

Style Augmentation. With the learned style representations from pretrained MeDUET, for cross-domain adaptation, we first build a style prototype from K unlabeled target-domain volumes:

$$\mathbf{s}^{\text{pro}} = \frac{1}{K} \sum_{i=1}^K \mathbf{s}^{(i)}. \quad (25)$$

To reduce sensitivity to the particular choice of K volumes and to track the empirical target distribution, we further update the prototype online using an EMA over target-domain mini-batches. During training, for each labeled source sample (\mathbf{z}, \mathbf{y}) , we stochastically generate a style-augmented volume in the MeDUET latent space. We keep the content tokens fixed and linearly mix the style tokens toward the target prototype with a random strength α :

$$\mathbf{s}' = (1 - \alpha) \mathbf{s} + \alpha \mathbf{s}^{\text{pro}}, \quad (26)$$

$$\mathbf{z}_{\text{aug}} = \mathcal{F}_{\text{dec}}(\text{conv}(\mathbf{c}, \mathbf{s}')). \quad (27)$$

where \mathcal{F}_{dec} is the decoder of MeDUET that reconstruct the patch tokens from factors, and conv denotes the convolutional layer used to aggregate factors. Let f_{θ} be the segmentation/classification network (UNETR in our experiments), for each mini-batch we optimize a combined supervised and consistency objective:

$$\mathcal{L}_{\text{sup}} = \mathcal{L}_{\text{task}}(f_{\theta}(\mathbf{z}), \mathbf{y}) + \lambda_{\text{aug}} \mathcal{L}_{\text{task}}(f_{\theta}(\mathbf{z}_{\text{aug}}), \mathbf{y}), \quad (28)$$

$$\mathcal{L}_{\text{cons}} = D_{\text{KL}}(\sigma(f_{\theta}(\mathbf{z}_{\text{aug}})) \parallel \sigma(f_{\theta}(\mathbf{z}))), \quad (29)$$

$$\mathcal{L} = \mathcal{L}_{\text{sup}} + \lambda_{\text{cons}} \mathcal{L}_{\text{cons}}. \quad (30)$$

where $\mathcal{L}_{\text{task}}$ is task loss for corresponding perception tasks, D_{KL} represents the KL divergence, σ is the softmax function, λ_{aug} and λ_{cons} are coefficients for balancing the loss term contributions. We apply latent style augmentation to a fraction p_{aug} of training samples per batch, drawing $\alpha \sim \mathcal{U}[\alpha_{\text{min}}, \alpha_{\text{max}}]$. Table 12 illustrates the hyperparameter settings of our style augmentation strategy under different label proportions.

D. Computational Analysis

Considering that the overall pretraining pipeline of our MeDUET is relatively complex, containing multiple components and loss terms, we provide a computational analysis to illustrate the practicality of our method. Specifically, we implement a compute cost and wall-clock time comparison with several Medical SSL methods [65, 79, 96] to ensure a fair comparison, as demonstrated in Table 13. Notably, all comparisons are conducted on identical pre-processing settings and the pretrain time is measured on four NVIDIA A100 GPUs. It can be observed that MeDUET achieves the best Dice/Accuracy while also enjoying the lowest Flops and per-epoch wall-clock time among all compared methods. This efficiency mainly comes from performing SSL in the VAE latent space with a $4\times$ spatial compression ratio, which greatly reduces the number of tokens processed by the ViT backbone. Hence, the overall pretraining time remains comparable to VoCo [79] and is substantially lower than MIM [96] and Hi-End-MAE [65], despite our more elaborate disentanglement objectives.

E. Experiments

E.1. More Ablation Study

Role of the VAE Tokenizer. To assess the sensitivity of MeDUET to the choice of VAE tokenizer, we further evaluate our framework using alternative VAE models. Given that tailored 3D VAEs for medical imaging remain relatively underexplored, we adopt the Patch-Volume Autoencoder from 3D MedDiffusion [69], a 3D VQGAN-based tokenizer pretrained on large-scale CT and MRI datasets. As shown in Table 14, replacing MAISI-VAE [24] with the Patch-Volume Autoencoder leads to only minor fluctuations in both synthesis and analysis performance. While MAISI-VAE achieves slightly higher averages, both tokenizers maintain consistently strong results, suggesting that the improvements of MeDUET arise primarily from the disentangled pretraining scheme rather than from any specific VAE design. These findings indicate that our framework is relatively insensitive to the tokenizer choice.

Factor Impact for Medical Synthesis Baselines. To further assess the usefulness of the learned factors, we replace the original metadata condition vectors in medical synthe-

Table 14. Ablation experiments on the role of VAE.

Method	Synthesis			Analysis			
	FID ↓	MMD ↓	MS-SSIM ↓	Dice Score (%)↑			
				BTCV		WORD	
	1-shot	100%	1-shot	100%			
Patch-Volume Autoencoder [69]	0.7948	0.5630	0.1686	78.55	94.13	79.29	94.22
MAISI-VAE [24]	0.7874	0.5598	0.1659	78.72	94.06	79.56	94.28

Table 15. Ablation experiments on the impact of our learned factor codes on baseline medical synthesis methods.

Method	FID ↓	MMD ↓	MS-SSIM ↓
MAISI [24]	0.9139	0.6292	0.2057
+ Factor Conditions (Ours)	0.9046 (-0.093)	0.6159 (-0.133)	0.1918 (-0.139)
3D MedDiffusion [69]	0.9216	0.6327	0.2032
+ Factor Conditions (Ours)	0.9081 (-0.135)	0.6198 (-0.129)	0.1931 (-0.101)

sis baselines [24, 69] with our pretrained content and style embeddings. As shown in Table 15, plugging in our factors yields consistent improvements on all three metrics for both baselines, even though the generative architectures and training setups are unchanged. This indicates that MeDUET provides richer and more informative conditioning signals than handcrafted metadata, capturing continuous, image-derived anatomy and appearance cues that are not fully described by discrete site labels, and can thus benefit a broad class of medical synthesis models.

E.2. Factor Generalization for MRI

To further demonstrate the generalization capability of our disentanglement scheme, we perform t-SNE visualization on the content and style factors extracted from the BraTS dataset [3], as shown in Fig. 9. On this out-of-distribution MRI dataset, the t-SNE plots reveal that the style embeddings form distinct clusters corresponding to the four MRI modalities (T1, T1ce, T2, FLAIR), whereas the content embeddings remain mixed across modalities. Notably, these BraTS modalities are never used as domain labels during pretraining. This emergent clustering indicates that our style branch automatically adapts to unseen modality-specific appearance factors, while the content branch remains modality-invariant. Together, these observations provide empirical evidence that the proposed disentanglement scheme generalizes beyond the supervised domains.

E.3. Failure Cases Analysis

Several failure cases of factor-guided synthesis with MeDUET are shown in Fig. 10. Typical qualitative failures include anatomically implausible shapes, missing or inac-

curate pathology representation, and incomplete content-style disentanglement. Below, we discuss several plausible causes and outline potential mitigation strategies: (i) In multi-center datasets, anatomical and pathological patterns often correlate with specific scanners or sites, causing the style branch to inadvertently learn anatomical cues. This issue may be alleviated by improving cross-center data balancing and introducing independence regularization between content factors and domain labels. (ii) Because content and style factors originate from a shared encoder and must satisfy strong reconstruction constraints, the model may redundantly store anatomical information in both branches. Stronger architectural separation, such as decorrelation constraints between branches, may help reduce this leakage. (iii) Joint optimization across multiple objectives can prioritize reconstruction fidelity over perfectly disentangled factor separation. In addition, extreme factor guidance during inference may push sampling into underexplored regions where residual entanglement becomes more apparent. Future work will investigate harder factor-swap sampling, as well as calibrated or regularized guidance ranges, to mitigate these effects.

F. Discussions

F.1. Exploration for Domain Setups

It is worth noting that not all datasets provide reliable style metadata (e.g., scanner vendor, field strength, kVp, reconstruction kernel). Consequently, we do not exploit such fine-grained style annotations; instead, we use dataset-level domain IDs as domain labels to ensure consistency across datasets. This choice is admittedly coarse, where each dataset may still contain multiple protocols and gradual shifts, but it roughly captures the dominant cross-dataset appearance differences that the style branch is meant to model. Because the style encoder learns a continuous style space under weak domain supervision, MeDUET does not rely on perfectly clean domains, and our experiments show that this simple labeling already yields stable disentanglement and strong performance, with finer-grained domain definitions left for future work.

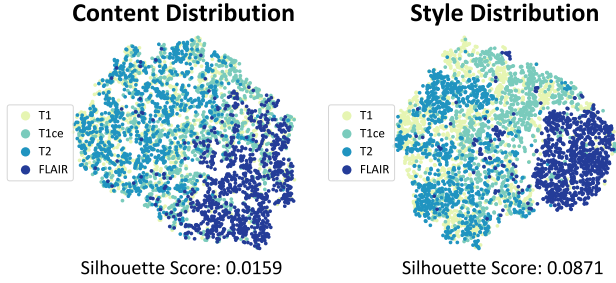


Figure 9. The t-SNE visualization of MeDUET content and style representations on the BraTS dataset, where points are color-coded according to their modality labels. Left: Content code distribution. Right: Style code distribution.

F.2. Empirical Factor Identifiability

We emphasize that our use of the term identifiability is purely empirical rather than theoretical. MeDUET does not provide formal guarantees that content and style factors are uniquely recoverable. Instead, we demonstrate approximate disentanglement through diagnostics such as domain linear probes, t-SNE visualizations, and factor-controlled generation. These results suggest that the learned domain-invariant content and domain-specific style spaces behave in a factorized manner under our training setup.

F.3. Limitations

While MeDUET demonstrates strong performance across diverse medical imaging tasks through a unified pretraining framework, several limitations remain. First, MeDUET introduces multiple components, increasing implementation complexity compared with simpler SSL baselines. Although operating in a compressed latent space keeps the computational cost and wall-clock time manageable, the overall pretraining pipeline remains resource-intensive. A promising future direction is to design lighter-weight objectives or distillation strategies that retain the learned factors while reducing architectural and training overhead. Additionally, our generative evaluation is primarily conducted on datasets sharing similar anatomical distributions as those used for pretraining. Cross-dataset or out-of-distribution synthesis is not extensively explored and warrants further investigation. Moreover, we currently focus on segmentation and classification as downstream analysis tasks. Extending MeDUET to other tasks such as detection, registration, or report generation, as well as to multi-institutional real-world data with heterogeneous protocols, is an important future direction.

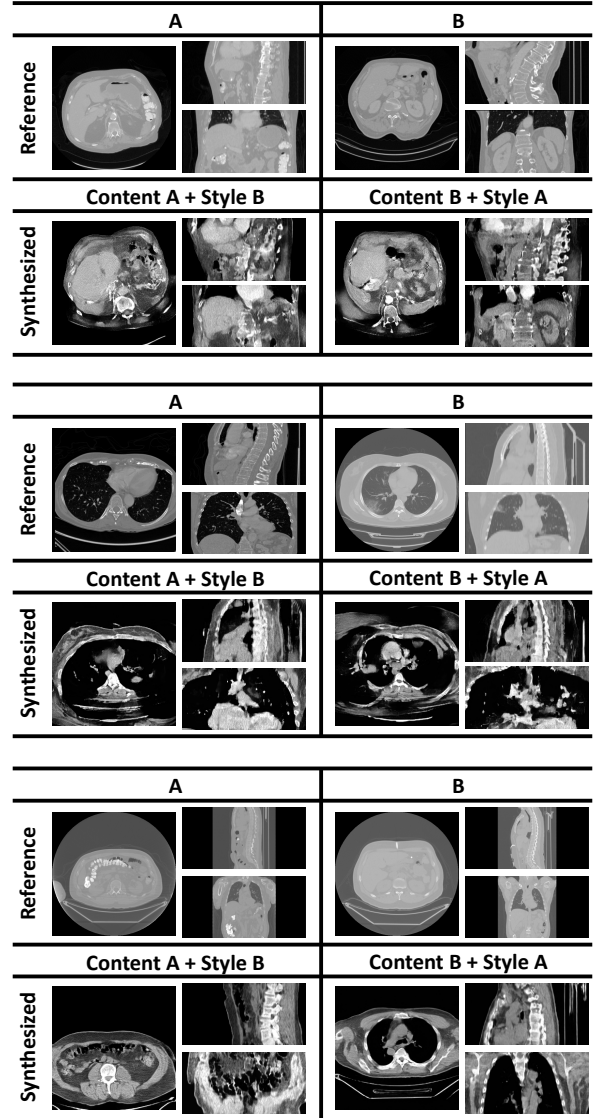


Figure 10. Some failure cases of synthesized images generated by MeDUET.